Contributions to Mineralogy and Petrology (2022) 177:21
https://doi.org/10.1007/s00410-022-01888-8

ORIGINAL PAPER

Experimental quantification of vanadium partitioning between eclogitic minerals (garnet, clinopyroxene, rutile) and silicate melt as a function of temperature and oxygen fugacity

Megan Holycross[1,2] · Elizabeth Cottrell[1]

Received: 10 September 2021 / Accepted: 6 January 2022

Abstract
Vanadium is a multivalent element that may speciate as V^{2+}; V^{3+}; V^{4+} and V^{5+} in silicate and oxide phases. The relative abundance of V in planetary materials can be used as a proxy for oxygen fugacity (fO_2) when its partitioning behavior has been calibrated with controlled laboratory experiments. Here we present the results of 20 piston-cylinder experiments executed over a 10-log unit range of fO_2 at temperatures from 800 to 1230 °C, at 1.8–2 GPa, to quantify the partitioning of V between garnet, clinopyroxene, rutile and hydrous silicate melt under conditions relevant to eclogite melting in subduction zones. In all experiments, the partitioning of V between phases is controlled nearly equally by fO_2 and by temperature (and/or compositional effects that are directly related to temperature). Vanadium is most compatible in experimental rutile, followed by clinopyroxene, then garnet. Calculated mineral/melt partition coefficients are ≥ 1 for all three phases in our experimental series. The high compatibility of V in eclogitic minerals results in negligible mass transfer of V during eclogite melting under all fO_2 conditions investigated. Oxidized species of V are more soluble in rutile compared to garnet and clinopyroxene, leading to a linear increase in rutile/cpx and rutile/garnet inter-mineral partition coefficients as fO_2 increases. We calibrate the partitioning of V among rutile-cpx and rutile-garnet pairs as an fO_2 proxy for natural rocks and test its application to eclogitic xenoliths from the Koidu kimberlite suite (Sierra Leone). Our application yields spurious fO_2 values for Koidu, indicating the V systematics of natural systems are likely much more complex than predicted by our experiments. Further work is needed to characterize the partitioning of V between eclogitic minerals over an extended range of mineral solid solutions, pressures, and temperatures before a V-oxybarometer may be applied to natural metamorphic systems with confidence.

Keywords Eclogite · Oxygen fugacity · Experimental petrology · Vanadium

Introduction

Vanadium is a first-row transition element that may exist in up to five valence states (V^0, V^{2+}; V^{3+}; V^{4+}; V^{5+}). The compatibility of V in silicate and oxide phases is determined by its valence and consequently by the oxygen fugacity (fO_2) imposed by the system. By taking advantage of V systematics, geoscientists have inferred the fO_2 of paleo (e.g., Canil 1997, 1999; Nicklas et al. 2016, 2019; Aulbach and Stagno 2016; Stolper and Bucholz 2019), modern (e.g., Shervais 1982; Lee et al. 2005; Laubier et al. 2014; Wang et al. 2019), and planetary (e.g., Righter et al. 2006; Nicklas et al. 2021) systems.

Inferences about fO_2 rely on quantification of the partition coefficient of V between phases, defined as

$$D_V^{A/B} = V \text{ in phase } A / V \text{ in phase } B \quad (1)$$

in controlled experiments over relevant ranges of temperature (T), pressure (P), composition (x) and fO_2 (e.g., Canil 1997, 2002; Canil and Fedortchouk 2001; Toplis and Corgne 2002; Mallmann and O'Neill 2009, 2013; Righter et al. 2011; Laubier et al. 2014; Arato and Audetat 2017; Shishkina et al. 2018; Sossi et al. 2018; Wang et al. 2019; Holycross and Cottrell 2020). Here we focus on quantifying

Communicated by Dante Canil.

✉ Megan Holycross
holycross@cornell.edu

[1] National Museum of Natural History, Smithsonian Institution, Washington, DC 20560, USA

[2] Department of Earth and Atmospheric Sciences, Cornell University, Ithaca, NY 14850, USA

Published online: 22 January 2022

D_V as a function of fO_2 under conditions relevant to subducting slabs and the roots of deep-seated arcs.

The relative distribution of V between eclogitic minerals (here, garnet, cpx ± rutile) has the potential to serve as an oxygen barometer, or oxybarometer, for natural rocks, provided all controls on V incorporation in grt, cpx and/or rt can be identified (e.g., Aulbach and Stagno 2016; Aulbach et al. 2019a; Aulbach 2020). Eclogite fO_2s are ill constrained, for both exhumed terranes and xenolith localities, in part from a shortage of applicable proxies. All published fO_2 proxies for eclogites are based on the thermodynamics of oxygen exchange reactions between mineral pairs (e.g., Zhao et al. 1999; Donohue and Essene 2000; Stagno et al. 2015).

Knowledge of V partitioning between eclogitic minerals is also critical for assessing the V systematics of arc magmas. Eclogitic minerals dominate slab assemblages in the sub arc region (Poli and Schmidt 2002), but also form in the roots of arcs where the overriding crust is thick enough to equilibrate high pressure cumulates (e.g., Ducea et al. 2015). Slab-top temperatures in roughly half of modern subduction zones reach the hydrous basalt + sediment solidus (e.g., Syracuse et al. 2010) and slab melting was likely more pervasive in hot Precambrian subduction zones (Martin 1986). Thus, V partitioning during slab melting may have a significant impact on the mass transfer of V throughout subduction zones.

The influence of fO_2 on V partitioning between eclogitic minerals and melt (i.e., rt/melt, cpx/melt and grt/melt) has been explored in a variety of separate studies but no study has simultaneously measured the relative incorporation of V in all phases in a single experimental series and at the P, T and x approaching those of natural eclogites. Here we present the results of piston-cylinder experiments designed to measure the partitioning of V during eclogite melting over a 10 log unit range of fO_2, from − 5 to + 6 log units relative to the quartz-fayalite-magnetite (QFM) buffer, at pressures from 1.8 to 2 GPa and temperatures from 800 to 1230 °C. Experiment fO_2s were controlled using two complementary O_2-buffering approaches and monitored using two independent techniques (Fe-XANES of the melt and the composition of Pt-Fe alloys). We report the partitioning of V between silicate melt, garnet, clinopyroxene and rutile to quantify mass transfer of V from subducting slabs to the overlying arc and evaluate the potential for the partitioning of V among mineral phases to be used as an eclogite oxybarometer.

Background and motivation

Vanadium oxybarometry utilizes the redox equilibria of four V oxide components as a proxy for fO_2 in geologic materials. In homogenous phases, the valence state of V is related to fO_2 through the electron exchange reactions.

$$2V^{2+}O + {}^{1}/_{2}O_2 = V_2^{3+}O_3 \quad (2)$$

$$V_2^{3+}O_3 + {}^{1}/_{2}O_2 = 2V^{4+}O_2 \quad (3)$$

$$2V^{4+}O_2 + {}^{1}/_{2}O_2 = V_2^{5+}O_5 \quad (4)$$

Direct measurements of V valence in geologic materials have mostly been restricted to silicate glasses, and there is limited information about V speciation in crystalline phases. X-ray absorption near-edge structure (XANES) spectroscopy on silicate glasses shows V valence increases rapidly over geologically relevant ranges of fO_2, shifting from V^{3+} to V^{4+} to V^{5+} over ΔQFM-3 to QFM + 4 (Sutton et al. 2005; Lanzirotti et al. 2018). Because different species of V have varying compatibility in silicate and oxide mineral phases, V concentrations in silicate and oxide phases should change as a function of fO_2 when T, P, and x are held constant.

However, if T, P and x are not static, these variables will also influence V speciation (in addition to fO_2). If the valence state of a redox couple approximates an equilibrium constant, the Clausius–Clapeyron relationship predicts more reduced species of V should be stable in melts at higher T (Schreiber 1986; Sutton et al. 2005). Sutton et al. (2005) reports a 10% reduction in V valence as T increases from 1275 to 1426 °C in a suite of isobaric ($\log fO_2 = -8$) CMAS glasses, amounting to a 6% reduction in V valence per 100 °C T increase. Likewise, if the molten oxides of V have differing partial molar volumes, P is also likely to impact the stable valence state of V; however, no published experimental study has investigated the effect of P on V speciation. The data of Sutton et al. (2005) suggest V speciation in high-temperature silicate glasses is generally not affected by variation in glass composition—with the exception of TiO_2, which appears to be negatively correlated with V valence in silicate glasses at constant T, P and fO_2.

Vanadium oxybarometry has been widely applied to determine the fO_2s of basaltic magmas (e.g., Lee et al. 2005; Laubier et al. 2014; Shiskina et al. 2018; Wang et al. 2019; Novella et al. 2020) and has promise as a redox proxy for metabasalts as well, although observations of V in geologic materials at the high pressures and low temperatures where eclogites equilibrate is more limited (Aulbach and Stagno 2016; Aulbach et al. 2019a, b; Aulbach 2020). Mid ocean ridge basalts contain on average 194–396 ppm V (Gale et al. 2013) and published whole rock measurements of V in subduction-related metabasalts bracket this spectrum (Barth et al. 2001; Hermann 2002). The similarity of bulk V in eclogites and MORB (the eclogite protolith) indicates V may be retained in solid residues during high T and P processing in subduction zones. Vanadium in eclogitic cpx and grt ranges in the 100s of ppm and concentrations of V in eclogitic rt often exceed 1000 ppm (e.g., Barth et al.

2001; Liu et al. 2014; Aulbach et al. 2019a)—concentrations that may be measured using accessible instrumentation like laser ablation inductively coupled plasma mass spectrometers (LA–ICPMS) or electron microprobes. Consequently, a V-based fO_2 proxy for eclogites may have two key advantages relative to other approaches: (1) it may be applied by anyone with access to commonly available analytical equipment; (2) loss of V from eclogites during melting or dehydration may be relatively limited such that the V composition of eclogites forms a coherent record of subduction zone fO_2 across a range of depths.

Methods

Experimental

We designed our experiments to meet the following goals (1) produce large melt pools in equilibrium with the eclogitic phases rt, cpx and grt; (2) establish phases with V contents that can be precisely measured using an electron microprobe; (3) maintain and quantify fO_2-buffered conditions.

We employed nine different starting materials over the course of our experimental campaign. All starting materials are tabulated in Table S1. The compositions of starting materials were varied in attempt to saturate in rutile at high T, to grow mineral grains large enough for electron microprobe analysis, to yield high experimental melt fractions, and to produce 'quenchable' homogeneous silicate melts suitable for chemical microanalysis. Our mixes generally have similar major elements compositions with significant variations in only TiO_2 and H_2O content. Four of our nine starting materials (mixes 1–4) were composed of silicate and oxide regents mixed in proportions to approximate the composition of a mid-ocean ridge basalt. 'Extra' TiO_2 was added to these mixes in values exceeding that of average MORB to promote rt saturation at high temperatures. Bulk TiO_2 concentrations ranged from 4.0 wt% in the highest temperature experiments to 2.1 wt% in the lowest temperature experiments. Five of the nine starting materials were mixed to form more evolved compositions (i.e., higher in SiO_2, lower in MgO and FeO). Melts in equilibrium with eclogitic assemblages become more silicic as T decreases due to increasing crystal fractionation (see Table S9). Using a more evolved bulk mix, crystals saturate with equilibrium melt compositions without the need for extensive crystal fractionation. This approach maximizes experiment melt fractions while maintaining saturation in the three key phases of interest.

We performed three early experiments using nominally dry starting materials and varied bulk water in subsequent experiments to promote the growth of large crystals and melt pools. Water was added to hydrated starting materials as $Al(OH)_3$ in proportions ranging from 1.8 to 5 wt% bulk H_2O, reducing Al_2O_3 in hydrous mixes to account for the additional Al_2O_3 produced by $Al(OH)_3$ decomposition. Vanadium was added to starting materials as V_2O_3. Four experiments were executed using starting materials with V_2O_3 doped at ~ 0.1 wt% (~ 600 ppm V). All other starting materials were doped with ~ 0.2–0.26 wt% V_2O_3 (~ 1300–1800 ppm V).

It is not possible to maintain constant fO_2 in high-P experiments because solid media assemblies are not closed systems. Changes in fO_2 may occur during mass transfer of Fe from experimental phases to noble metal capsule walls, while H_2 may be added to or lost from the experiment via diffusion through capsule walls. We attempted to control experiment fO_2s using two complementary approaches, employing both Fe-saturated Pt containers (Davis and Cottrell 2021) and 'double capsule' assemblies where the interior capsule contains the system of interest and the exterior capsule contains an fO_2-buffering mineral assemblage (Eugster 1957). Both capsules must be saturated with water vapor (activity of H_2O (a_{H2O}) = 1) to be buffered at the nominal fO_2 of the mineral assemblage.

We performed all experiments in Pt capsules pre-saturated with Fe, with the exception of one experiment run at the Ru-RuO_2 buffer which employed a pure Pt container. To pre-saturate capsules, we cut 2 mm diameter Pt tubes (1.64 mm or 1.4 mm ID) and placed them in a 5 cm diameter Pt crucible containing a flux of 75 wt% Fe_3O_4- 25 wt% $LiBO_4$, mixed in proportions such that the activity of Fe_3O_4 in the flux was buffered at unity. Loaded crucibles were covered with Pt lids and hung the crucible from an Al_2O_3 cane in the hotspot of a controlled-atmosphere furnace set at 1300 °C. A CO–CO_2 gas mix was piped into the furnace in proportions to saturate Pt at the desired X_{Fe} (mole fraction Fe) according to the calibration of Kessel et al. (2001) at 1300 °C. The furnace fO_2 was set before saturation runs using a using a ZrO_2 sensor referenced to pure O_2 and was measured again after run completion. FePt tubes were cleaned in warm HCl, neutralized and sonicated in H_2O. Pre-saturated tubes contained X_{Fe} = 0.05–0.35. Clean FePt tubes were fashioned into capsules, loaded with starting material and welded shut with a PUK welder. Fabricated FePt capsules were typically 5 mm long and contained 6–12 mg of starting material depending on capsule volume (i.e., ID). We ran seven experiments using a single FePt capsule (i.e., with no exterior capsule containing an O_2 buffer).

We executed thirteen experiments using the 'double capsule' technique (Eugster 1957). In these experiments, the interior capsules of pre-equilibrated FePt alloy, fabricated as described above, were loaded with hydrous starting material and welded shut. These were loaded into an exterior 3-mm OD Au or $Au_{90}Pd_{10}$ capsule along with a solid oxygen buffer and liquid H_2O. The solubility of H_2O in solid mineral buffer

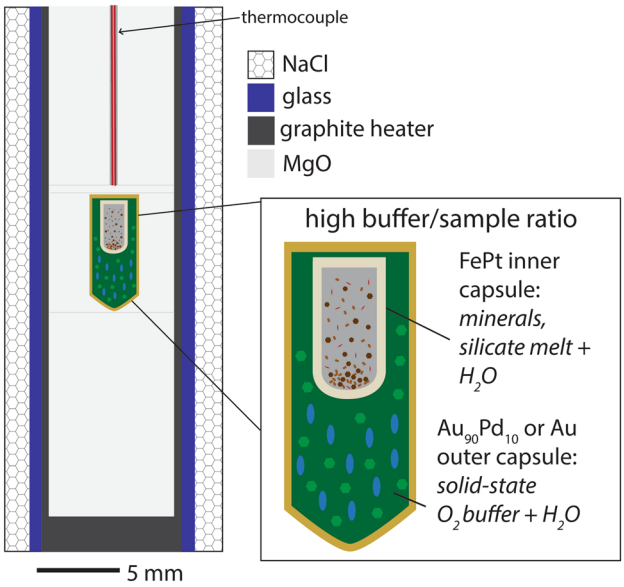

Fig. 1 Piston-cylinder assembly for NaCl-Pyrex® runs. $BaCO_3$ runs were similarly proportioned but used $BaCO_3$ as a pressure medium without a glass cylinder separating the graphite heater from the exterior *P* medium

phases is sufficiently low that a_{H2O} is unity in the exterior capsule under all run conditions. Exchange of hydrogen between capsules indirectly sets the fO_2 of the interior capsule through the reaction.

$$H_2O(aq) = H_2 + {}^1/_2\,O_2 \quad (6)$$

Buffer material was loaded in the outer capsule at a ratio of 10:1 relative to starting material. Typical weights were ~ 6–12 mg of starting material in the interior capsule and ~ 60–80 mg of buffer material in the exterior capsule. Double capsules were weighed after spot welding and placed in a 110 °C furnace for at least 1 hour. Capsules that showed signs of water loss were discarded. We used six different types of fO_2 buffering assemblages in our experimental series (Fe-FeO, Ni-NiO, SiO_2-Fe_2SiO_4-Fe_3O_4, MnO-Mn_3O_4, Fe_3O_4-Fe_2O_3, Ru-RuO_2).

Sealed capsules were placed in ½" diameter piston-cylinder assemblies. Graphite heaters and MgO crushable pressure media were used in all assemblies. $BaCO_3$ was used as a hydrostatic pressure media in 13 experiments and NaCl-Pyrex® was used in 7 experiments. All assemblies were wrapped with Pb foil. $BaCO_3$-bearing assemblies were subject to a friction correction calibrated to the melting point of NaCl (Akella et al. 1969) that amounted to roughly 20% at run pressure. NaCl-Pyrex® assemblies were assumed to be frictionless. Full details of all experiment assemblies are published in Table S2. Figure 1 shows a typical double-capsule experimental assembly employed here.

Loaded experiments were cold pressurized to 1.8 GPa before heating. Experiment temperatures were ramped at a rate of 100 °C/min while simultaneously increasing *P* to the final run condition. All experiments were ramped up to 30 °C above the final equilibration *T*, annealed for 1 h and then cooled at 6 °C/h to the final equilibration *T*. This slow cooling step was introduced to help promote the growth of large crystals while avoiding inducing an overly large thermal (and consequently, compositional) gradient during anneal. All experiments were quenched isobarically by holding pressure constant while shutting off the power.

Experiments were performed at $T = 800$–1230 °C and $P = 1.8$–2 GPa. Experimental durations were proportional to *T* and ranged from ~ 2 days at the highest temperatures to ~ 12 days at 800 °C. Run conditions are reported in Table 1. Completed experiments were mounted in epoxy, exposed in cross section and polished for analysis. All experiments were made into thin sections to examine run products in the third dimension and determine their suitability for characterization with XANES spectroscopy.

Analytical

EPMA

We measured the chemical compositions of all experiments using the JEOL 8530F Hyperprobe at the National Museum of Natural History. Si, Ti, Al, Fe, Mn, Mg, Ca, Na, K and V in experimental minerals and melts were measured using an accelerating voltage of 10 kV and current of 20 nA. Fe and Pt in experiment capsule walls were measured in traverses using an accelerating voltage of 15 kV and current of 20 nA. A subset of experiments were reanalyzed using the Cameca SXFive electron microprobe at Syracuse University. We do not report any analyses of V that fell below twice the calculated detection limit (*DL*) of our probe routine (average $DL = 66$ ppm; we do not report V < 132 ppm from EPMA measurements) and any analyses of crystalline phases that appeared to be contaminated by melt or by secondary fluorescence of nearby rutile. Full details of our electron microprobe analytical routines, including measurements of secondary standards, are reported in the Supplementary Tables.

The electronic properties of Ti and V are extremely similar, which presents an obstacle for accurate measurement of V in Ti matrices using X-ray analytical techniques (microprobe, XRF, XANES). While mass spectroscopy offers improved resolution of V from Ti, our experimental mineral grains are too small to be analyzed using commonly available MS techniques that require large (≥ 10 µm) spot sizes. Consequently, the best option for characterizing V in experimental mineral phases was the electron microprobe. Accurate measurement of V in Ti-bearing materials on the microprobe requires a correction to account for the overlap

Table 1 Experiment run conditions and phase equilibria

Expt#	*P*	*T* (°C)	t (*h*)	Mix used	fO_2 approach	Solid buffer used	Measured log f_{O2} ΔQFM[1]	+ log f_{O2} error	− log f_{O2} error	Modal proportions[2]				
										Hydrous melt	grt	cpx	rt	Other
1	2	1200	92	1	Single capsule	–	− 1.0	0.5	0.7	48	27	24	–	–
2	2	1200	96	1	Single capsule	–	− 1.1	0.6	0.6	16	34	44	3	fsp
4	2	1230	73	1	Single capsule	–	− 0.1	0.5	0.5	17	29	49	2	fsp
9	1.8	1150	61	4	Double capsule	Ni-NiO	0.1	0.6	0.6	56	32	12	–	–
14	2	1025	20	2	Single capsule	–	0.6	0.6	0.6	49*	28	19	3	vap
19	2	1025	48	3	Double capsule	Fe_3O_4-Fe_2O_3	4.2	0.4	0.4	42*	27	27	3	psb, vap
20	2	1100	79	3	Single capsule	–	1.7	0.5	0.5	58	17	23	2	vap
22	2	1050	50	5	Single capsule	–	0.3	0.6	0.6	50	21	21	3	qtz
23	2	1050	45	5	Single capsule	–	− 1.8	0.7	0.7	50	21	21	3	qtz
24	2	1050	84	5	Double capsule	MnO-Mn_3O_4	3.3	0.5	0.3	53	16	24	2	qtz
27	2	950	71	6	Double capsule	Fe_3O_4-Fe_2O_3	4.7	0.4	0.4	58	17	17	4	qtz
31	2	950	66	6	Double capsule	Ni-NiO	− 1.2	0.8	0.8	52	28	16	3	qtz
35	2	850	91	5	Double capsule	SiO_2-Fe_2SiO_4-Fe_3O_4	− 1.1	0.8	0.8	44	17	17	2	qtz, ky, amph, vap
37	2	850	68	7	Double capsule	Fe-FeO	− 4.3	0.9	0.9	72	11	9	2	qtz, opx, vap
38	2	875	115	7	Double capsule	MnO-Mn_3O_4	3.7	0.7	0.8	65	6	15	2	qtz, opx, psb, vap
39	2	850	67	5	Double capsule	Ni-NiO	− 2.0	1.0	1.1	56	23	19	3	vap
40	2	825	93	8	Double capsule	Ni-NiO	− 1.5	0.9	0.9	67	8	10	2	qtz, opx, vap
45	2	800	295	9	Double capsule	Fe-FeO	− 5.4	0.9	0.9	75	10	8	2	amph, vap
46y	2	900	69	8	Double capsule	Ni-NiO	− 1.6	0.7	0.7	59	12	15	2	qtz, vap
47	2	1050	45	5	Double capsule	Ru-RuO_2	6.3			43	26	26	–	rhom. oxide, vap

*Includes both melt and 'quench mat'

[1] f_{O2} from FePtO thermo referenced to QFM buffer from Frost et al. (1991)

[2] abbreviations after Whitney and Evans (2010)

of the Ti Kβ peak with the VKα peak (Snetsinger et al. 1968). The result of this overlap is that, if left uncorrected, Ti Kβ X-rays will be erroneously attributed to V Kα, yielding V concentrations that are higher than 'true' values. This effect scales as a function of Ti weight fraction in the matrix but can be overcome using a simple correction if Ti-bearing, V-free certified reference materials are available for analysis. Although this overlap correction is routine in many EPMA software packages, we emphasize that deploying the correction in a systematic fashion is critical for accurate results. Repeat analysis of experimental materials on the NMNH and Syracuse microprobes using different analytical routines, but the same Ti/V overlap correction routine, yielded nearly identical results. The correction routine we employed is covered in detail in the Supplemental Material.

LA-ICP-MS

We used the LA-ICP-MS-MS in the Cornell University Mass Spectrometry and Spectroscopy (CMaS) Facility to measure V in a subset of our experimental glasses. The CMaS Facility houses an ESI NWR 193UC-HE excimer laser coupled to an Agilent 8900 ICP-QQQ-MS-MS. Laser data were collected in single quadrupole mode. All experimental glasses were ablated at a fluence of 4 J/cm^2 and a 10 Hz rep rate using either a 40 or 20 µm circular spot depending on the size of the melt pools. NIST610 glass (Jochum et al. 2011) was used as the standard for glass analyses with USGS glasses (Jochum et al. 2005) used as secondary standards. LA-ICP-MS data were reduced in the Iolite software package using ^{29}Si as the internal standard in the trace element data reduction scheme. Samples were ablated for 30 s, followed by 30 s in which background was collected. Standards bracketed ablation of unknowns and were run every ten samples. He was used as the carrier gas for the laser aerosol. Chemical data for all experiments are reported in the Supplemental Material.

Fe-XANES

We used Fe K-edge XANES spectroscopy to determine the $Fe^{3+}/\Sigma Fe$ ratios of glasses from the six experiments bearing large-enough glass pools for analysis with a defocused beam. We collected Fe-XANES spectra at GSECARS beamline 13-ID-E at the Advanced Photon Source over four sessions using the methods of Cottrell et al. (2009) and Cottrell et al. (2018). We collected spectra in fluorescence mode from 7012 to 7492 eV using a Si [311] monochromator. We repeatedly analyzed Cottrell et al. (2009) reference glass LW_0 to monitor and correct for instrument drift between sessions. We calculated $Fe^{3+}/\Sigma Fe$ ratios from the area-weighted centroids of experimental glasses using the andesite calibration of Zhang et al. 2016 corrected for the effect of recoilless fraction on the Mössbauer spectra of glass standards (Zhang et al. 2018).

We lowered the photon flux density to minimize beam damage by placing sheets of aluminum foil upstream of the incident beam and by defocusing the beam to a 25 µm^2 or 50 µm^2 square spot. The resulting photon flux densities during XANES analysis ranged from 5×10^5 to 9.5×10^5 photons/s/µm^2. The need for large, clear melt pools > 25 µm^2 limited XANES analyses to 6 of 20 total experiments.

Our glasses are low in FeO* (0.5–4.5 wt%) and extremely water-rich (4–18 wt% H_2O by difference). This places them at high risk for photo oxidation from beam damage during XANES analysis. Cottrell et al. (2018) showed that, although photo oxidation can occur during analysis of hydrous glasses at flux densities as low as 3×10^6 photons/s/µm^2, hydrous basalt glass standards analyzed at flux densities $< 6\times10^7$ photons/s/µm^2 return $Fe^{3+}/\Sigma Fe$ ratios within error of their Mössbauer-determined $Fe^{3+}/\Sigma Fe$ ratios when applying the calibration of the anhydrous glass standard suite of Cottrell et al. 2009. Because our glasses are a different composition, and exceeded the water concentration range tested by Cottrell et al. 2018, we ran two independent tests on hydrous glass standards in all sessions to ensure we were collecting XANES data under damage-free conditions. Outcomes of the beam-damage tests are reported in the Supplementary Material.

Results

Phase equilibria

Figure 2 displays backscattered electron images of representative experiments. We employed a chi-squared minimization to calculate modal mineral proportions on a hydrous basis (Table 1). Results of our mass balance calculations show discrepancies between Na_2O in the starting materials and Na_2O in run products, indicating Na was lost from the glass during electron microprobe analysis, partitioned into a fluid phase at high pressures, or both (e.g., Bai and Koster van Groos 1999; Sisson and Kelemen 2018).

Seventeen experiments co-saturated in cpx, grt and rt. Three experiments saturated in grt and cpx but not rt. Modal proportions of grt and cpx are similar in all experiments (Table 1). Experimental grts are mostly pyrope (0.44–0.64) with subequal almandine (0.14–0.35) and grossular (0.15–0.23) components. One experiment run at 800 °C and ΔQFM-5.4 yielded a high-Fe grt with the composition $Alm_{0{\cdot}64}Py_{0{\cdot}8}Grs_{0{\cdot}15}$. Clinopyroxene compositions are diopside-rich (0.75–0.95) with increasing jadeite component at high temperature. Silicate melt is present

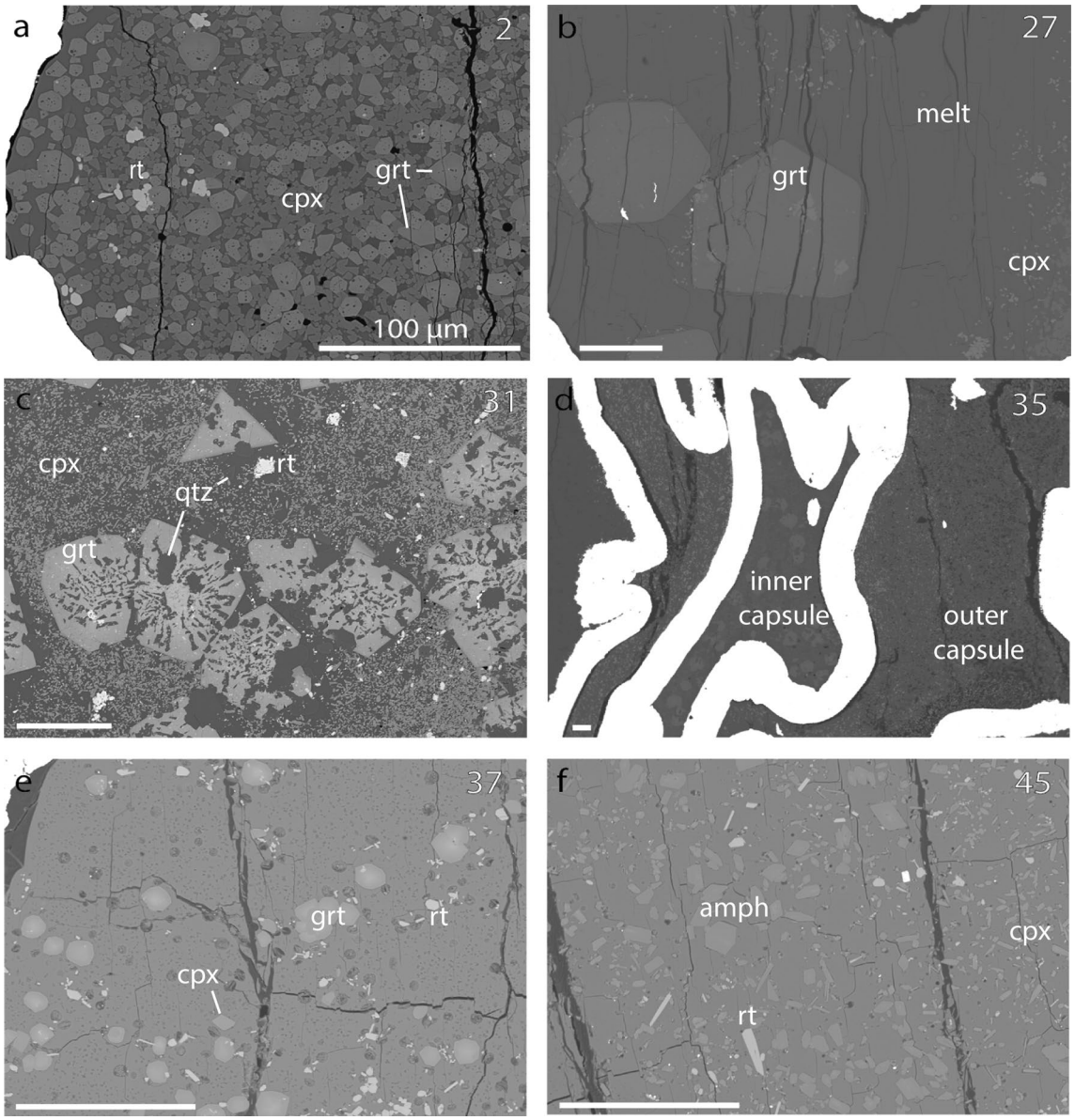

Fig. 2 Backscatter electron images of experimental run products. White scale bar is 100 µm in all images. Experiment number is printed in the top left corner in each image. Runs using nominally dry starting materials yielded higher crystal fractions (**a**) compared to runs using hydrous starting materials (**b**–**f**). Figure 2d shows a double capsule run using a high buffer-sample ratio. Glasses often contained quenched bubbles (**e**, **f**) suggesting a separate vapor phase may have been present at high *P*

in all runs, with melt fractions greater than 40% in all experiments except for two high-*T* experiments run using nominally dry starting materials. A large volume of silicate melts in two experiments run at 1025 °C quenched to a 'mat' of dendritic crystals and glass. We observed some heterogeneous nucleation of crystals upon quench in these experiments.

Buffer assemblages in double-capsule runs were inspected post-experiment and the presence of both phases was visually confirmed (Table 1). Even with all buffer phases present, the fO_2s of our experiments still deviated from nominal buffer fO_2s (see following sections). In these cases, the buffer phases may still be present simply due to sluggish reaction kinetics at relatively low temperatures.

Eleven experiments produced silicate glasses with quenched bubbles, indicating melts contained a separate vapor phase at high pressure. The water contents of our glasses range from 4 to 18 wt%, calculated using the 'water by difference' method. Very high H_2O contents were calculated for many experiments; however, the water by

difference method has been shown to overestimate the true water contents of glasses by 0.5–2 wt% (Hughes et al. 2019). Quantitative determination of H_2O in our silicate glasses via Fourier transform infrared spectroscopy is precluded by the small volumes of our experiment capsules. We prepared all experiments as thin sections epoxied to Fe-free glass slides to enable XANES analysis, with little to no experimental material leftover to prepare free glass wafers.

Some experiments also included combinations of plagioclase, Fe-Ti oxides, quartz, orthopyroxene, kyanite and amphibole. Plagioclase is present in two experiments run using a nominally dry starting material. Fe-oxide phases, including psuedobrookite, saturated in our most oxidized experiments ($\geq \Delta QFM+3$). Orthopyroxene, kyanite and amphibole appeared in experiments at $T \leq 875$ °C. The chemical compositions of all phases are tabulated in the Supplemental Material.

Vanadium partition coefficients

We calculated the standard error on V partition coefficients from:

$$\sigma = D_V^{A/B} \times \sqrt{\left(SD/V\right)_A^2 + \left(SD/V\right)_B^2}.$$

where σ is the standard error, SD is the standard deviation of multiple EPMA or LA-ICP-MS analyses of V in each phase. Calculated mineral/melt partition coefficients and standard errors for rt, grt and cpx are reported in Table 2. Partition coefficients for all other phases present in our experiments are reported in Table S7. The low concentrations of V in many of our silicate melts and small size of the melt pools (which precludes collection of LA-ICP-MS data) limits the calculation of $D_V^{min/melt}$ to 12 of our 20 experiments. $D_V^{min/melt}$ was calculated using LA-ICP-MS analyses of silicate melt where available. The standard errors of $D_V^{min/melt}$ calculated using EPMA analyses of V in silicate melts are 2–2.5 greater than values calculated using LA-ICP-MS data due to the larger standard deviation of EPMA analyses which approached the detection limit of our analytical routine.

Determination of experiment fO_2s

We calculated fO_2s from XANES determinations of $Fe^{3+}/\Sigma Fe$ ratios in six experimental glasses using the empirical parameterization of Kress and Carmichael (1991). The standard error of the algorithm of Kress and Carmichael (1991) was calculated by Cottrell et al. (2021) to be ± 0.56 log units and is the largest source of uncertainty in calculating experiment fO_2s from Fe-XANES analyses.

We constrained the fO_2s of our experiments using an additional independent method (modified from Davis and Cottrell 2021) based on the equilibrium thermodynamics of the Fe in our Fe-Pt alloy capsules and FeO in our silicate melts. Experiment fO_2 is related to Fe in the capsule alloy and FeO in the silicate melt by

$$Fe_{alloy} + {}^1/_2\, O_2 = FeO_{melt} \quad (7)$$

$$f_{O_2}\Delta IW = 2log\left(\frac{X_{FeO_{melt}}}{X_{Fe_{metal}}}\right) + 2log\left(\frac{\gamma_{FeO_{melt}}}{\gamma_{Fe_{metal}}}\right) \quad (8)$$

where $fO_2\Delta IW$ is oxygen fugacity relative to the iron-wustite buffer (Frost 1991). Multiple EPMA measurements of the capsule wall directly in contact with silicate melt were used to calculate the average molar fraction of Fe in the alloy (XFe_{alloy}). The activity coefficient (γ) of Fe in the capsule alloy was calculated from Eq. 11a of Kessel et al. (2001) modified with Eq. 3 of Gudmundsson and Holloway (1993)

Table 2 Mineral/melt partition coefficients for cpx, grt and rt

Expt#	log f_{O2} ΔQFM	T (°C)	V cpx/melt*	SE	V grt/melt*	SE	V rt/melt*	SE
1	− 1.0	1200	**4.1**	0.9	**2.8**	1.1		
4	− 0.1	1230	**2.2**	0.1	**1.4**	0.2	**6.9**	1.6
9	0.1	1150	**5.4**	0.3	**2.7**	0.2		
19	4.2	1025	2.3	1.3	1.3	0.8	20.7	11.4
20	1.7	1100	**1.9**	0.5	**1.3**	0.2	**10.7**	0.6
22	0.3	1050	**9.9**	0.4	**6.4**	1.0	**53.2**	3.8
24	3.3	1050	**2.3**	0.4	**1.9**	0.4	**18.8**	0.6
27	4.7	950	**2.7**	0.5	**2.3**	0.2	**23.9**	0.3
31	− 1.2	950	13.9	6.3	8.0	3.7	58.7	28.8
35	− 1.1	850	10.4	5.2	7.6	3.8	60.9	29.4
38	3.7	875	1.1	0.4	1.0	0.3	13.7	3.5
40	− 1.5	825	18.1	3.4	10.7	2.8	88.2	15.3

This table includes only experiments in which silicate melts could be analyzed for V

*Bold font denotes LA-ICP-MS values used for melt

to correct for the effect of pressure on γFe. The mole fraction of FeO in silicate melt ($XFeO_{melt}$) was determined directly by XANES, or when XANES measurements were not available, was calculated iteratively from EPMA measurements of total FeO to account for the contribution of Fe_2O_3 (e.g., Barr and Grove 2010). The mole fraction of Fe in silicate melt ($XFeO_{melt}$) was calculated on an anhydrous basis. The activity coefficient of FeO in silicate melts was calculated using the approach of O'Neill and Eggins (2002) and was corrected for temperature using γFeO_{calc}*(1673/T), where T is experiment temperature in K. The greatest sources of uncertainty in fO_2s calculated using this method are the standard deviation of measurements of FeO in our silicate melts and the estimated errors of the calculated values of Eq. 11a of Kessel et al. (2001). Both terms are accounted for in our quoted fO_2 uncertainties. All parameters used in the calculation of experiment fO_2s are reported in the Table S4.

Figure 3 demonstrates the excellent agreement in experiment fO_2s calculated from two independent methods. Because we quantified melt $Fe^{3+}/\Sigma Fe$ ratios in a fraction of our experiments, but calculated fO_2s from alloy-melt equilibria for all experiments, we use only experiment fO_2s calculated from FePtO equilibria throughout our discussion for internal consistency. We note that the fO_2 of Experiment 47 was not measured because Fe solubility in Pt is negligible at the Ru-RuO_2 buffer (O'Neill et al. 2006). Further discussion of experiment fO_2 is located in the Supplement.

Approach to equilibrium

The general lack of crystal zoning in BSE images, the low standard deviation of repeat EPMA analyses, and the systematic partitioning relationships derived from our experiments suggest they are chemically homogeneous. The trace element content of our starting materials is similar to or lower than previous V-partitioning studies that demonstrate agreement with Henry's law (Canil, 1997, Canil and Fedortchouk 2000; Mallmann and O'Neill, 2009; Laubier et al., 2014; Shishkina et al., 2018; Wang et al., 2019). The excellent agreement between fO_2s derived from glass $Fe^{3+}/\Sigma Fe$ ratios and FePtO equilibria demonstrates silicate melts and capsule wall edges are in close approach to redox equilibrium. Our experiments were designed to saturate eclogitic minerals with large (> 40%) melt fractions; because the melts generally dominated the experimental assemblages—even though melt pools between crystalline phases may be small (Fig. 2)—the crystal phases should be equilibrated at the same redox condition as the melt. Davis and Cottrell (2021) show their FePt alloy capsules record the same fO_2 as glass $Fe^{3+}/\Sigma Fe$ ratios and spinel-oxybarometry performed on the same experiments. Because we have adopted a key aspect of Davis and Cottrell's approach, and because of the good agreement between glass $Fe^{3+}/\Sigma Fe$ ratios and FePtO equilibria, we expect all phases in our experiments to record the same fO_2 conditions.

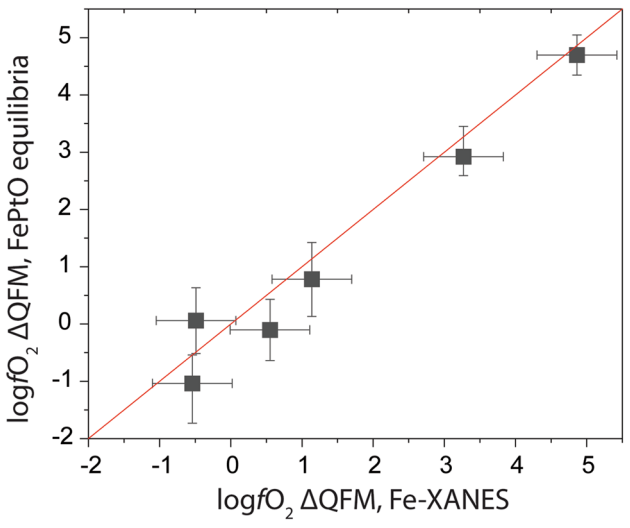

Fig. 3 Agreement between experiment fO_2s calculated using two independent methods. Red line shows perfect agreement between calculated fO_2s (1–1 line)

Iron and other siderophile elements present in our experiment may alloy with Pt capsules. This effect is amplified under reducing conditions where the stability of Fe^0 is enhanced. We used a Fe_3O_4-flux to saturate Pt capsules with Fe in proportions calculated to approach equilibrium between Fe_{alloy}-FeO_{melt} at the desired fO_2 in high-*P* runs. This leaves our experiments open to both Fe loss and Fe gain from capsule walls. While mass transfer of Fe from silicate melts to the capsule walls has occurred in our experiments (see Table S4), this is process has not impacted our results or interpretations. Fe mass transfer in our experiments is in fact advantageous because it suggests that the Fe_{alloy}-FeO_{melt} equilibria is sensitive to variations in fO_2 at experimental timescales, validating our approach for calculating fO_2. The good agreement between fO_2s calculated with two independent methods (Fe-XANES and Fe_{alloy}-FeO_{melt}) indicates our experiments approached fO_2 equilibrium over the long run times employed, despite some initial mass transfer between the capsule and melt/minerals.

Similarly, noble metal capsules in piston-cylinder assemblies are also open to H_2 exchange with their surroundings. We see evidence for both gain and loss of H_2 (as H_2O) in our experimental melt compositions—for instance, runs that used the nominally H_2O-free starting material were found to have water-bearing silicate melts. Double-capsule experiments that are not H_2O-saturated in the interior capsule (i.e., $a_{H2O} < 1$) will be buffered at fO_2 below the solid media O_2 buffer contained in the outer capsule. We calculated a_{H2O} in our silicate melts using the model of Burnham (1975), reported in Table S8. While

the Burnham model is calibrated to only 1 GPa, it provides a reasonable estimate of a_{H2O} in our experiments in the absence of models calibrated to higher *P*. Calculated water activities are low ($a_{H2O} < 0.4$) for runs that used nominally dry starting materials; calculated a_{H2O} in all other experiments extends from 0.58 to > 1. We note that quenched vapor bubbles are present in experiments with calculated $a_{H2O} < 1$ (Table 1). This indicates the vapor bubbles may be the products of exsolution on quench; the vapor bubbles may contain CO_2 or other gases in addition to water vapor; and/or the Burnham (1975) model is not suitable for extrapolation to our high-*P* melts. Although calculated a_{H2O} is frequently < 1 in our experiments, we observe generally good agreement between measured fO_2s and the nominal fO_2s of the solid buffers used in double-capsule runs. Further details are reported in Table S2 and Section S4.

Vanadium becomes siderophile under conditions relevant to core formation, with metal solubility increasing as fO_2 decreases and temperature increases (Wood et al. 2008; Siebert et al. 2011, Fischer et al. 2015). This raises the possibility that V may have alloyed with Fe-Pt capsules during high *P* runs. However, in the colder, and more oxidizing experiments of this study, we do not observe V loss to the capsule. All EPMA measurements of V in capsule walls are below the detection limit of our analytical routine, indicating that negligible V has alloyed with Fe-Pt containers during high *P* runs. Mass balance calculations of V in experimental run products return the concentration of V in our starting materials within acceptable error.

Discussion

Phase chemistry

We utilized nine different starting materials in our experimental series. Although many of the starting materials vary only slightly in their major element chemistry (Table S1), this raises the possibility that the composition of our final phases equilibrated at high *T* and *P* may not be relevant to natural eclogite melting scenarios and/or may deviate substantially from the results of previous experiments that equilibrated eclogitic phases at similar conditions.

We collated data from eclogite melting experiments run using nominally basaltic starting materials at 1.6–2.5 GPa and 750–1160 °C for comparison with our results (Table S9). Despite the use of more evolved starting materials in our experiments and the greater variety in starting material compositions, the chemistries of our anhydrous silicate melts plot within the range of reported experimental melts generated from basaltic starting materials. Our silicate melt compositions closely follow the temperature trends defined by the literature data. This indicates the variation in starting materials we employed did not yield spurious results.

Silicate melt

Experimental eclogite melt compositions become more polymerized (expressed as the ratio of non-bridging oxygens to tetrahedrally coordinated cations, NBO/T; Mysen 1983) as *T* decreases (e.g., Rapp and Watson 1995). The NBO/T ratio of our experimental silicate melts decrease from 0.42 to 0 as *T* decreases from 1230 to 800 °C, consistent with previous work. Silicate melts in our hottest experiments are lower in SiO_2 and higher in FeO* and MgO compared to melt compositions in our coldest experiments, which are hydrous rhyolites. Rutile-saturated melts contain the least TiO_2 at low *T* (Ryerson and Watson 1987). We note this trend because the concentration of TiO_2 in silicate melts may influence trace element partitioning into crystalline phases (Xirouchakis et al. 2001; Schmidt et al. 2004; Dygert et al. 2013; Leitzke et al. 2016; Holycross and Cottrell 2020).

Vanadium concentrations in silicate melts vary as a function of fO_2 and *T* with hot, oxidized melts containing the most V. Silicate melts in reduced, cold experiments typically contain ≤ 130 ppm V, twice the detection limit of our probe routine. Our calculated $D_V^{min/melt}$s are limited to experiments buffered at fO_2s > ΔQFM-1.5 where there was adequate V in the melt for probe measurements, or there were large enough melt pools for LA-ICP-MS measurements. All silicate melt data are tabulated in Table S8.

Clinopyroxene

Clinopyroxene has the formula $M2M1T_2O_6$, where the M2 site is 6- or 8-coordinated and the M1 site contains 6-coordinated +2, +3 or +4 cations with atomic radii ranging from 0.53- 0.83 Å (Cameron and Papike 1981). Previous work shows V substitutes in cpx on the M1 site (Karner et al. 2008; Papike et al. 2014). Trivalent V may directly exchange with Al^{3+} or Fe^{3+} in cpx, but the incorporation of more oxidized species of V requires coupled substitution mechanisms to maintain crystal charge balance.

We report $D_V^{cpx/melt}$ for 12 experiments equilibrated at 825–1230 °C and ΔQFM-1.5 to +4.7. Cpx/melt partition coefficients for V are plotted as a function of experiment fO_2 in Fig. 4. We find V is compatible in cpx under all experimental conditions, with our coldest, most reducing experiments yielding the greatest values of $D_V^{cpx/melt}$. In general, $D_V^{cpx/melt}$ decreases as fO_2 increases, consistent with the interpretation that more oxidized species of V are less compatible in cpx (Canil and Fedortchouk 2000; Toplis and Corgne 2002; Karner et al. 2008; Mallmann and O'Neill 2009;

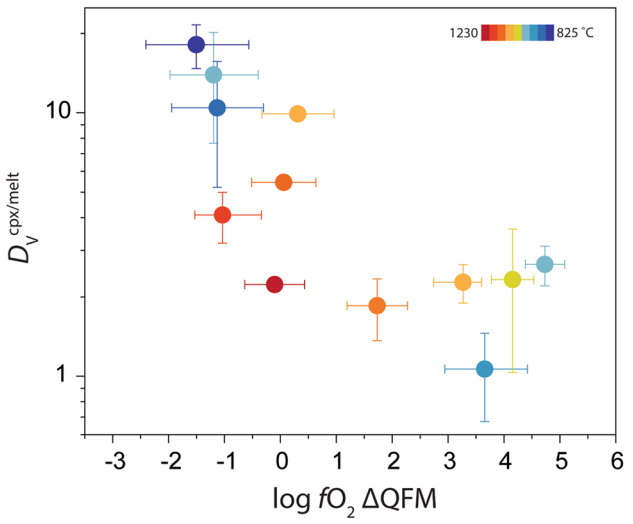

Fig. 4 Variation in $D_V^{cpx/melt}$ as function of fO_2 with colored contours for experiment temperature. Cold, reducing experiments produced the highest values of $D_V^{cpx/melt}$

Papike et al. 2014; Wang et al. 2019) but fO_2 cannot solely explain the range of $D_V^{cpx/melt}$ measured in our experiments.

We investigated the influence of four parameters (fO_2, T, cpx composition and melt composition) on V solubility in cpx. A linear regression of $D_V^{cpx/melt}$ against experiment fO_2 shows redox state accounts for only 50% of the variance in V partitioning behavior. The additional control(s) on $D_V^{cpx/melt}$ may be cast in terms of T or x (melt; cpx); however, because T directly influences the chemistry of minerals and melts, these variables cannot be changed entirely independently in our experiments. $D_V^{cpx/melt}$ increases down temperature in experiments executed at roughly the same fO_2, in agreement with Wang et al. (2019). It is not clear if this apparent T effect is exclusively due to the positive entropy of fusion of the V-bearing cpx endmember (Blundy and Wood 1997) or if it is a secondary effect of changing composition as T decreases. Silicate melts in low T experiments are significantly more polymerized than high T experiments (Table S9), and trace element partitioning studies consistently show $D^{min/melt}$ increases as melt polymerization increases (e.g., Gaetani 2004). Holycross and Cottrell (2020) also theorized increasing TiO_2 in silicate melt compositions depresses V partitioning into oxide phases, raising the possibility that a similar effect may be observed for silicate minerals. TiO_2 solubility is directly related to T and melt polymerization (e.g., Ryerson and Watson 1987; see Table S10). We measured the highest values of $D_V^{cpx/melt}$ in experiments with the least TiO_2 in the melt phase; these experiments also contain the most polymerized melt compositions equilibrated at the lowest T. All three parameters (T, NBO/T or melt TiO_2) are statistically significant controls on $D_V^{cpx/melt}$ with p-values < 0.003. However, regressing $D_V^{cpx/melt}$ against fO_2 and more than one of these parameters results in multicollinearity because T, NBO/T and melt TiO_2 are not independent variables in our experiments. The result is generally the same whether the second variable (in addition to fO_2) is cast in terms of T, NBO/T or melt TiO_2—each in isolation accounts for ~ 30% of the variance in $D_V^{cpx/melt}$.

Crystal field effects will also impact the incorporation of trace elements in cpx. Clinopyroxene forms complex solid solutions with compositions that shift in response to variations in P, T and fO_2. Previous work shows Al-rich pyroxenes incorporate greater amounts of trace elements than equivalent Al-poor compositions (Lundstrom et al. 1994; Gaetani and Grove 1995; Hill et al. 2000; Wood and Blundy 2001; Pertermann and Hirschmann 2002; Adam and Green 2006; Francis and Minarik 2008; Bedard 2014; Beard et al. 2019; Mollo et al. 2020). This effect has been attributed to the presence of increased Al on the tetrahedral site, which helps to balance the charge mismatch incurred by the incorporation of tri-, tetra- or pentavalent cations in cpx. Previous work by Karner et al. (2008) and Papike et al. (2014) suggests the primary exchange mechanism for tri- and tetravalent V is through charge balance with 4-coordinated Al ± 8-coordinated Na through the reactions

$$^{VI}V^{3+} + {}^{IV}Al^{3+} = {}^{IV}Si^{4+} + {}^{VI}M1^{2+} \quad (9)$$

$$^{VI}V^{4+} + {}^{VIII}Na^{+} + {}^{IV}Al^{3+} = {}^{IV}Si^{4+} + {}^{VI}M1^{2+} + {}^{VIII}M2^{2+} \quad (10)$$

High temperature and low silica activity promote the substitution of Al on the tetrahedral site (Kushiro 1960). Increasing fO_2 may also increase total Al and ^{IV}Al in cpx (Green and Pearson 1985; Adam and Green 1994; Mollo and Vona 2014; Beard et al. 2019). The net effect is that all species of Al are most abundant in cpx in hot, oxidized rocks low in silica.

We fingerprinted the substitution mechanism of V in our experiments by examining the relationship between $D_V^{cpx/melt}$ and the major element chemistry of cpx. We began with an investigation of the influence of fO_2 and T on the major element composition of cpx. We do not observe strong correlations between fO_2 and any cation component in cpx apart from V. Partitioning of Mg, Fe, Ca and Ti between cpx and melt increases as temperature drops (see complete cpx data in Table S10). Al partitioning in cpx falls as T decreases and melt polymerization and silica activity increase, consistent with previous interpretations. Although the solid solution nature of cpx results in correlations between $D_V^{cpx/melt}$ and several cations in cpx, we identify total Al as the most statistically significant compositional parameter (p value = 0.0002) in a regression of cpx components vs. $D_V^{cpx/melt}$. Oxygen fugacity and total Al (in atoms per formula unit, or apfu) together account for 90% of the variance in $D_V^{cpx/melt}$ —an improvement of 10% relative to regressions including fO_2

and T, NBO/T or melt TiO_2. Al in cpx is covariant with T, NBO/T and melt TiO_2. The remaining variance in our new values of $D_V^{cpx/melt}$ may be a result of fitting our data with a linear regression as opposed to a function that considers the stoichiometry of the V–O redox reactions (e.g., Eq. 15 in Mallmann and O'Neill 2009). Regardless of the functional form of our expression, it describes nearly all the observed variance in $D_V^{cpx/melt}$. More details on our choice of fitting technique may be found in the Supplementary Materials.

The significance of Al in our regression indicates that (1) variations in Al in cpx track changes in T and/or melt composition; and (2) the presence of Al in cpx is strongly related to the relative compatibility of V. Previous work (e.g., Karner et al. 2008; Papike et al. 2014; Wang et al. 2019) suggests increased Al/^{IV}Al should enhance the solubility of V in cpx, while we observe the opposite—a strong negative correlation between $D_V^{cpx/melt}$ and Al. We also find fO_2 accounts for only about half of the variance in $D_V^{cpx/melt}$.

The negative correlation between V and Al suggests V may directly exchange with Al in cpx through the reaction

$$^{VI}V^{3+} = {}^{VI}Al^{3+} \quad (11)$$

Alternatively, the negative correlation between V and Al in our experiments may represent a shift to an Al-deficient cpx structure in which V is more compatible. The M1 octahedron is a critical building block in the cpx lattice that impacts both the configuration of the M2 polyhedron as well as the kinking of linked tetrahedral chains (e.g., Cameron and Papike 1981). The size of the M1 octahedron is controlled by the size of the cation occupying the site. Previous work shows the ideal M1 site radius decreases as Fe^{3+} replaces Al in cpx (i.e., along the jadeite-aegirine join; Redhammer et al. 2006). All valence states of equivalently coordinated V have ionic radii smaller than Fe^{3+} and larger than Al (Shannon 1976). This suggests aegirine-rich compositions may be able to incorporate greater amounts of smaller, highly charged V relative to jadeite or other cpx solid solutions with larger M1 sites.

We anticipate the abundance of Fe^{3+} will impact V solubility in cpx in natural eclogites, independent of V's formal valence state. We looked to a series of five experiments executed at ΔQFM-1 ± 0.5 and 825–1230 °C to examine the relationship between Fe and V in our experiments under constant redox conditions. Although we were not able to directly measure the concentration of Fe^{3+} in our experimental cpx (only total Fe), the presence of Fe^{3+} in cpx will result in an increase in calculated total Fe. There is a very strong positive correlation between $D_V^{cpx/melt}$ and $D_{Fe}^{cpx/melt}$ and a very strong negative correlation between $D_V^{cpx/melt}$ and $D_{Al}^{cpx/melt}$ in our experiments executed at relatively constant fO_2 (Fig. 5). The correlation is in part a result of the T dependencies of each cation: Fe and V become relatively enriched in cpx down temperature, while Al becomes relatively depleted. All cpx compositional data are reported in Table S10.

We compiled $D_V^{cpx/melt}$ from experimental studies that either controlled (i.e., through a gas-mixing furnace) or monitored (i.e., through use of a redox sensor) fO_2 to assess if our new findings extend to the literature data (Table S11). We further culled the literature data to consider only experiments run at fO_2 = ΔQFM-2 to +2.5, where the relationship between $D_V^{cpx/melt}$ and fO_2 is approximately linear (Bedard 2014). Our compiled dataset includes 59 partition coefficients from six studies (Canil and Fedortchouk 2000; Toplis and Corgne 2002; Mallmann and O'Neill 2007, 2009; Wang et al. 2019; this study) at T = 825–1560 °C and P = 0.001–3 GPa. We find fO_2, P, T and Al in cpx (expressed as either total Al or ^{IV}Al, calculated as [^{IV}Al = 2-Si]) are all statistically significant controls on $D_V^{cpx/melt}$ and together account for 83% of the variance in our compiled $D_V^{cpx/melt}$ dataset. We note only 11% of the variance in our regression is controlled by fO_2. The relationship between Al/^{IV}Al and $D_V^{cpx/melt}$ across 59 experiments is strongly negative—increasing Al/^{IV}Al is correlated with decreasing $D_V^{cpx/melt}$, consistent with our new observations. Our experiments heavily influence the compositional trend in our compiled global dataset;

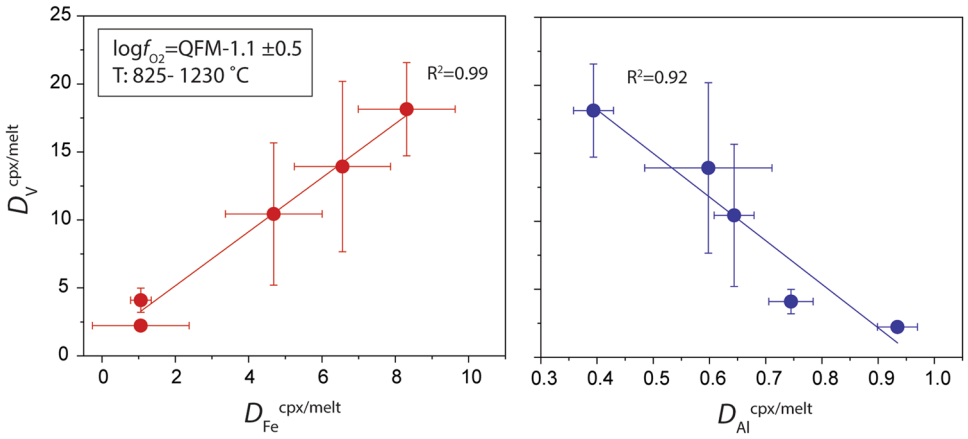

Fig. 5 Relationship between Fe, Al and V partitioning between cpx and melt in experiments at constant fO_2. $D_V^{cpx/melt}$ increases as the partitioning of total Fe in cpx increases and Al decreases

separate regressions of the same literature data without our new values of $D_V^{cpx/melt}$ (51 values) do not yield a statistically significant dependence on ^{IV}Al or total Al. Our result contrasts with that of Wang et al. (2019), who found ^{IV}Al was an important control on $D_V^{cpx/melt}$ in multiple linear regressions of much the same literature data we parameterize here. The negative correlation of Al/^{IV}Al and V in cpx in our parameterization is simply explained by their opposite geochemical behavior: Al/^{IV}Al is most abundant in cpx at high T, high fO_2 and low silica activity, while the V is most abundant in cpx at low T, low fO_2 and high silica activity. We did not find any correlation between Fe and V in cpx in our compiled literature data set but note that some of the included studies used Fe-free starting materials (Canil and Fedortchouk 2000; Mallmann and O'Neill 2007, 2009), which may obscure any apparent trends.

Our calculated $D_V^{cpx/melt}$ are significantly higher than previously reported values (Table S11). We attribute the offset between our new data and the literature values to the difference in experimental conditions. We executed our experiments over a greater range of T and at higher Ps than other studies. Consequently, the composition of minerals and melts in our experiments are distinct from those of previous studies, and these parameters critically influence V partitioning between cpx and melt.

In sum, our experiments suggest that over a wide variety of conditions relevant to eclogite melting, $D_V^{cpx/melt}$ is nearly equally controlled by fO_2 and by cpx composition (which is itself a function of T, P and fO_2). Our analysis of the literature data indicates the influence of fO_2 on $D_V^{cpx/melt}$ over ΔQFM-2 to + 2.5 is relatively minor compared to thermal effects across a broader spectrum of experimental P–T–x. Al and ^{IV}Al are negatively correlated with V in our experiments because these two elements exhibit opposite geochemical behavior in cpx-melt systems. We predict the solubility of V will be enhanced in Fe^{3+}-rich cpx relative to other solid solutions.

Garnet

Garnet has the general formula $X_3Z_2Si_3O_{12}$, where X is a dodecahedral site that hosts divalent cations like Mg, Ca, Fe^{2+} and Mn, and Z is an octahedral site hosting trivalent cations like Al, Fe^{3+} and Cr. Previous work demonstrates V^{2+} and V^{3+} are compatible in grt and substitute on the Z site via reaction 11 (Ohtani et al. 1989; Righter et al. 2011). The incorporation of V^{2+} requires the substitution of additional cations, like Ti or Si, to charge balance the exchange of V^{2+} for Al^{3+} (Righter et al. 2011). Righter et al. (2011) also showed the average valence of V in peridotite grt is limited to 2.46–2.55 in rocks equilibrated at ΔQFM − 4.5 to − 1.8, with no correlation between V valence and fO_2. This result suggests redox state may not be the dominant control on V valence in garnet.

We report $D_V^{grt/melt}$ for 12 experiments equilibrated at 825–1230 °C and ΔQFM − 1.5 to + 4.7 (Fig. 6). The coldest, most reduced experiments yielded the greatest values of $D_V^{grt/melt}$. Vanadium is compatible in grt under all but the hottest, most oxidized conditions, where it becomes neutral. We executed multiple linear regressions to investigate the influence of four parameters (fO_2, T, grt composition and melt composition) on V compatibility in grt in our experiments. We find fO_2 accounts for 47% of the variance in calculated $D_V^{grt/melt}$, and either T, NBO/T or melt TiO_2 can account for an additional 39% of the variance in our garnet partitioning data (total $R^2 = 0.86$). We do not identify any statistically significant relationships between $D_V^{grt/melt}$ and grt composition across our integrated experimental dataset. The remaining variance in $D_V^{grt/melt}$ may be attributed to the use of a linear regression to fit our data as opposed to a function that considers the stoichiometry of the V–O redox reactions.

The absence of a clear compositional influence on $D_V^{grt/melt}$ could indicate multiple host sites for V in grt that shift as a function of f_{O2} and/or T. We looked to a group of five experiments executed at an average f_{O2} of ΔQFM-1 (± 0.5) and T = 825–1230 °C to investigate the substitution mechanism for V in grt under constant redox conditions (all grt data are tabulated in Table S12). We find a very strong ($R^2 = 0.93$) negative correlation between $D_V^{grt/melt}$ and T over this range, consistent with results from our broader data set. $D_{Mn}^{grt/melt}$, $D_{Mg}^{grt/melt}$ and $D_{Al}^{grt/melt}$ are also negatively correlated with T ($R^2 \geq 0.83$) and are consequently

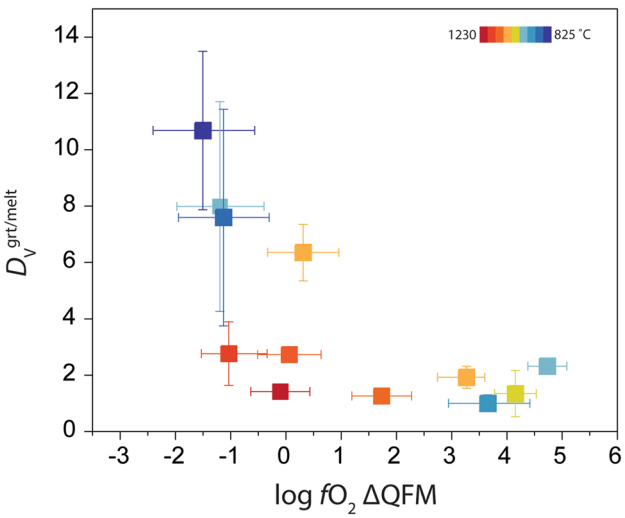

Fig. 6 $D_V^{grt/melt}$ plotted as a function of fO_2 with T contours. Cold, reducing experiments produced the greatest values of $D_V^{grt/melt}$. Vanadium is compatible in grt in all but the hottest, most oxidizing experiments, where it becomes neutral

positively correlated with $D_V^{grt/melt}$. Previous work has found increasing grossular content enhances trace element solubility because the large ionic radius of Ca imparts high strain on the dodecahedral site (Armbruster and Geiger 1993; Ballaran et al. 1999), easing the incorporation of size-mismatched trace elements on the octahedral site. However, we find only a weak positive correlation between $D_V^{grt/melt}$ and Ca or grossular content in our experiments.

We aggregated published values of $D_V^{grt/melt}$ from the literature for comparison with our new data (Table S13). We selected $D_V^{grt/melt}$ from experiments where fO_2 was controlled or measured and restrict our analysis to experiments executed over the fO_2 range ΔQFM − 2 to + 2.5 ($n = 18$; $T = 825–1450$ °C; $P = 1.8–3$ GPa; Mallmann and O'Neill 2007; Wang et al. 2019; this study). Oxygen fugacity explains only 16% of the variance in our compiled $D_V^{grt/melt}$, with the majority of the variance in the dataset (75%) accounted for by T. Combined with P, these 3 variables explain 91% of the variance in the 18 values of $D_V^{grt/melt}$. We do not find any grt compositional variables to be a statistically significant in a regression against our compiled literature values of $D_V^{grt/melt}$.

Our new experiments combined with our analysis of the literature suggest V partitioning between grt and melt may be most strongly controlled by T, with fO_2 and P as secondary influences. Although we cannot identify a specific substitution mechanism for V in grt from our mineral/melt partitioning data, it is likely to substitute for Al on the octahedral site as predicted by Ohtani et al. (1989) and Righter et al. (2011).

Rutile

Rutile is an oxide with the non-stochiometric formula TiO_{2-x} ($x = 0 – 0.02$). Rutile may incorporate V via direct exchange for Ti and through coupled substitutions with hydrogen, trivalent or pentavalent cations:

$$V^{3+} = Ti^{3+} \quad (12)$$

$$V^{3+} + H^{+} = Ti^{4+} \quad (13)$$

$$V^{3+} + (Nb, Ta)^{5+} = 2Ti^{4+} \quad (14)$$

$$V^{4+} = Ti^{4+} \quad (15)$$

$$V^{5+} + \left(Al^{3+}, Cr^{3+}, Fe^{3+}\right) = 2Ti^{4+} \quad (16)$$

Rutile possesses semiconducting and photocatalytic properties that are tied to its concentration of point defects, which are negatively correlated with absolute fO_2 (e.g., Bak et al. 2012). Because the absolute fO_2s of solid-state oxygen buffers decrease strongly down temperature, point defects are by far most abundant in our coldest (and most reducing) experiments. The formation of a point defect in rt also creates a free electron, which is then available to help balance the incorporation of charge-mismatched ions in TiO_2. This may be an important mechanism for accommodating V^{5+} in rt. Colasanti et al. (2011) also note that rt in hydrous systems can take in substantial amounts of H^+. The presence of H^+ in rt could provide a means to charge balance the exchange of V^{3+} with Ti^{4+} in our experiments or may stabilize more reduced species of V in rt under high fO_2s through intervalence charge transfer (Colasanti et al. 2011).

Holycross and Cottrell (2020) measured the partitioning of V between rt and three silicate melt compositions in one atm experiments run at 1300 °C and varying fO_2. Their data show V compatibility in rt under isothermal conditions is strongly dependent on both fO_2 and melt composition. At a given fO_2, $D_V^{rt/melt}$ increases as melt polymerization increases and melt TiO_2 decreases (melt TiO_2 is covariant with NBO/T). Comparing the results of Holycross and Cottrell (2020) to studies executed at conditions more relevant to subduction zones where fO_2 was not measured shows $D_V^{rt/melt}$ rises considerably at higher P and lower T (Foley et al. 2000; Xiong et al. 2005).

We report $D_V^{rt/melt}$ for 10 experiments run at 825–1230 °C and $fO_2 = \Delta QFM - 1.5$ to + 4.7. Vanadium is strongly compatible in rt over the entire fO_2 and T range of our experiments, with $D_V^{rt/melt}$ extending from 7 up to 88 (Fig. 7). Vanadium is most soluble in rt in relatively reduced, cold experiments, matching the trends observed for $D_V^{grt/melt}$ and $D_V^{cpx/melt}$. We examined the influence of three parameters (fO_2, T, melt composition) on $D_V^{rt/melt}$ with multiple linear regressions. As emphasized previously, composition and T are not independent variables in our experiments. Oxygen fugacity explains roughly 50% of the variance in $D_V^{rt/melt}$, while either T or NBO/T can account for an additional 30% of the variance. We also tested the dependence of $D_V^{rt/melt}$ on melt TiO_2 content—which we again note does not change

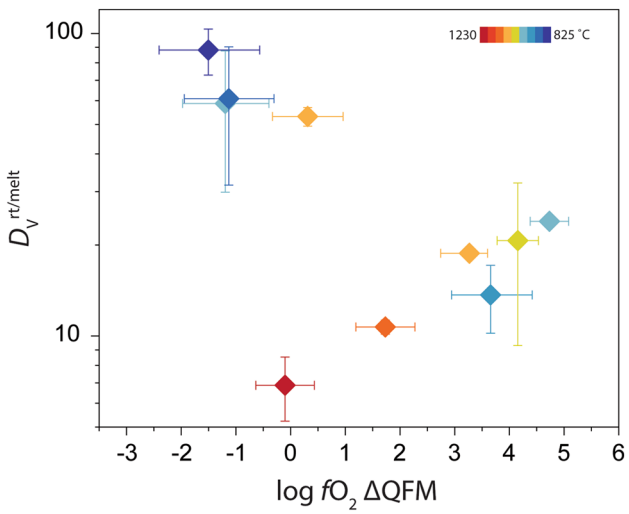

Fig. 7 Variation of $D_V^{rt/melt}$ as a function of fO_2 plotted with contours for experiment T. Like cpx and grt, V is most compatible in rt in our coldest, most reducing experiments; however, $D_V^{rt/melt} >> 1$ even under very oxidizing conditions

independent of T and NBO/T. This regression yielded the best fit to our data, with fO_2 and melt TiO_2 accounting for 90% of the variance in $D_V^{rt/melt}$. All rt compositional data are reported in Table S14.

Holycross and Cottrell (2020) found NBO/T and melt TiO_2 could account for equal parts of the variance in $D_V^{rt/melt}$ measured at 1300 °C and 1 atm, with elevated $D_V^{rt/melt}$ observed at low NBO/T and low melt TiO_2. The melt compositions in Holycross and Cottrell (2020) contained TiO_2 in concentrations that greatly exceeded terrestrial values (up to 20 wt%) because their experiments were run at low P and high T where rt is highly soluble in silicate melts. Because $D_V^{rt/melt}$ is likely to correlate with any component that alters NBO/T, Holycross and Cottrell (2020) preferred to cast NBO/T as the independent variable in their regression. Our new, high-pressure melts are substantially lower in TiO_2 (0.25–5.2 wt%) compared to the melts of Holycross and Cottrell (2020), yet TiO_2 still appears to have a vital role in the partitioning of V between rt and melt. The addition of melt TiO_2 to our multiple linear regression significantly improved the R^2 of our parameterization. This suggests that even small amounts of Ti in silicate melt may influence the behavior of V in rt-melt systems. See the discussion in Holycross and Cottrell (2020) for further details.

We examined shifts in the trace element composition of rt at constant redox conditions in four experiments executed at an average fO_2 of ΔQFM-1 (±0.5) at T = 825–1230 °C. $D_V^{rt/melt}$ is negatively correlated with T (R^2 = 0.92) while the concentration of Al in rt (and $D_{Al}^{rt/melt}$) is positively correlated with T (e.g., Hoff 2019). Consequently, there is a negative relationship between $D_V^{rt/melt}$ and Al in our experiments at QFM-1, suggesting Al and V occupy the same site in rutile. We did not observe any other robust correlations between $D_V^{rt/melt}$ and rt composition in this subgroup of experiments.

We note that the concentration of total Fe in all experimental rt is a strong function of fO_2 and does not appear to be T dependent (e.g., Bromiley et al. 2004). Rutile FeO* increases from 0.19 wt% to 5.7 wt% over a ~ 10 log unit increase in fO_2, indicating the solubility of Fe^{3+} in rt is enhanced relative to Fe^{2+}. The presence of Fe^{3+} also provides a coupled substitution mechanism for charge balancing V^{5+} in rt under oxidizing conditions.

In sum, the elevated concentrations of V in rt and very high $D_V^{rt/melt}$ measured across our experiments suggests all species of V are remarkably compatible in rutile. Rutile-melt partitioning of V in our new experiments is generally greater than measured $D_V^{rt/melt}$ in the high T, 1 atm experiments of Klemme et al. (2005); Mallmann et al. (2014) and Holycross and Cottrell (2020) at comparable fO_2s. Our new values are in the same range as previous high-P data reported by Foley et al. (2000) and Xiong et al. (2005) in experiments where fO_2 was not monitored or controlled. The enhanced solubility of V in rt in our high P, lower T, hydrous experiments is likely due to a combination of factors, including thermal impacts, availability of H^+ for charge balancing under hydrous conditions, decreased TiO_2 in experimental melts, and a positive relationship between P and $D_V^{rt/melt}$ due to a volume change that favors substitution of the smaller ions of V^{5+} and V^{4+} for Ti^{4+} and V^{3+} for Ti^{3+} (Shannon, 1976).

Other phases

We calculate $D_V^{opx/melt}$ in two experiments run at 825 °C and ΔQFM − 1.5; and 875 °C and ΔQFM + 3.7. Orthopyroxene incorporates V at roughly half the level of cpx at the same conditions, consistent with the results of Wang et al. (2019). The partitioning of V between amphibole and melt is roughly equivalent to $D_V^{cpx/melt}$ in a single experiment at 850 °C, ΔQFM − 1. Two experiments equilibrated at ΔQFM + 3.7 and + 4.2 stabilized pseudobrookite, while one experiment run at ΔQFM + 6.3 precipitated an Fe–Ti–Al rhombohedral oxide. We find V is highly compatible in all oxide phases; the concentration of V in pseudobrookite is roughly equivalent to the concentration of V in rutile in experiments where both phases are present. Kyanite was identified in one experiment at 850 °C and ΔQFM-1.1. Vanadium in kyanite is below the concentrations of V in cpx, rt, grt and amph from the same run. Vanadium in quartz and feldspar from all experiments is present at concentrations below the detection limit of our EPMA analytical routine, indicating V is incompatible in these phases. Compositional data for these phases is located in Table S14.

Potential for mass transfer of V during eclogite melting

Constraints on the potential for mass transfer of V during eclogite dehydration and melting are critical for assessing the V systematics of arc magmas and other subduction zone rocks. Our experimentally determined $D_V^{min/melt}$s for eclogitic phases are significantly higher than values reported in the literature for experiments conducted on peridotitic compositions at equivalent fO_2s, but at higher T and lower P. The high compatibility of V in cpx, grt and rt in our experiments, which target the P–T-x conditions relevant to eclogite melting, implies that V will be strongly retained in solid residues during eclogite melting in subduction zones. Previous work has demonstrated V is immobile during the dehydration of sediments and metabasalts (Green and Adam 2003; Spandler et al. 2007).

We parameterized our new values of $D_V^{rt/melt}$, $D_V^{cpx/melt}$ and $D_V^{grt/melt}$ as a function of fO_2 and T to model the V compositions of eclogite melts of varying mineral assemblages at 780 °C, 2 GPa and fO_2s from ΔQFM-2 to + 3. We modeled the V concentration of 5% batch melts of eclogites with equal proportions of grt and cpx ± 1–3 mode% rt (Table S16

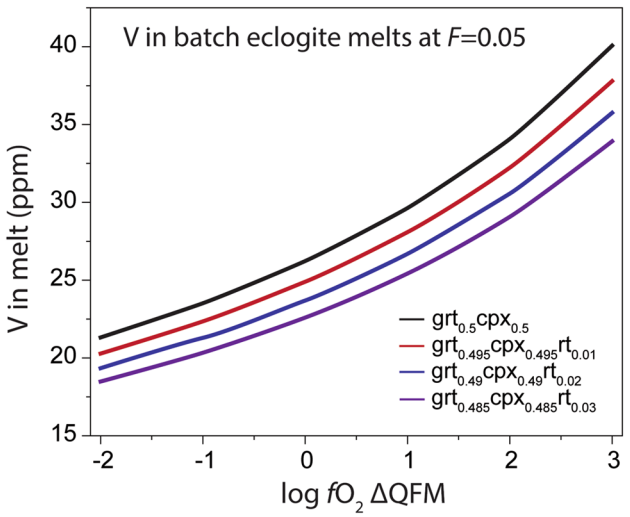

Fig. 8 Modeled concentrations of V in 5% batch eclogite melts of varying mineral assemblages at 780 °C and 2 GPa plotted as a function of fO_2. The concentration of V in eclogite melts is low (≤40 ppm) at all fO_2s and mineral modes. Our results imply melts of eclogites or melts that fractionate arc cumulates in subduction zones will be depleted in V relative to melts of the surrounding arc mantle under all model conditions

and Fig. 8). Assuming a concentration of 309 ppm V in the eclogite protolith (Gale et al. 2013), the concentration of V in eclogite melts is relatively low (≤40 ppm) across all fO_2s and for all mineral modes we considered. Varying fO_2 from ΔQFM − 2 to ΔQFM + 3 drives a 2 × increase in melt V; the effect of changing mineral mode is subtle compared to fO_2. Our analysis also demonstrates that the fractionation of deep-seated arc cumulates will yield melts depleted in V relative to melts of the surrounding arc mantle (e.g., Mallmann and O'Neill 2013; Wang et al. 2019).

Our simple model suggests that arc rocks that incorporate slab melts (adakites) should be relatively depleted in V compared to rocks derived solely from peridotite melting. We compiled and filtered mineral inclusion data from the PetDB database to see if adakites record the influence of low-V slab melts. We searched PetDB (www.earthchem.org/petdb) on 10, December 2021, for adakitic melt inclusions using search parameters guided by Defant and Drummond 1990: rock type = igneous + volcanic + mafic; analyzed material = inclusion; with chemistry = V analyzed + 15 < Al_2O_3 < 23 wt%; 42 < SiO_2 < 56 wt%, 400 < Sr < 10,000 ppm, Y < 18 ppm. We compared the compositions of adakitic inclusions to those of melt inclusions in the same SiO_2 (42–56 wt%) and MgO (5–7 wt%) range (Table S17). The V contents of adakitic melt inclusions (avg = 207 ppm; SD = 40, n = 19) are roughly 33% lower than V in non-adakitic melt inclusions (avg = 310 ppm; SD = 78; n = 27). The observed depletion of V in the adakitic melt inclusions is consistent with the results of Sisson and Kelemen (2018), who estimated partial melts of subducting basalt in the eclogite facies may constitute 1/3 to 1/10 of the final parental arc magma. This result indicates the low abundance of V in adakitic inclusions may be in part due to the mixing of a V-depleted slab melt component with melts of the surrounding mantle.

Relative partitioning of V between mineral phases

Our experiments were designed to measure the relative incorporation of V in garnet, clinopyroxene and rutile at varying fO_2 under slab-like conditions. Consequently, the partitioning of V between minerals ($D_V^{min/min}$) in our experiments could be parameterized for use as an empirical oxybarometer if all controls on V partitioning between phases are identified. The advantages of a trace-element-based redox proxy for eclogites are many. Such a barometer could be applied to both older, dry xenoliths and younger, hydrous exhumed terranes, forming an internally consistent and contiguous record of subducting slab fO_2s across space (i.e., depth) and time. Measurement of V in these common phases via microprobe and LA-ICP-MS is more accessible for most labs than spectroscopic measurement of $Fe^{3+}/\sum Fe$.

Clinopyroxene and garnet crystallize shallowly during subduction and are stable to great depth in the mantle. Rutile is an accessory mineral in eclogites; by definition, its modal abundance is far below clinopyroxene or garnet. Thus, it may appear more practical to parameterize the partitioning of V between cpx and grt for use as an oxybarometer because these phases are more common in eclogites. However, cpx and grt both prefer to incorporate V in its reduced forms (V^{2+} and V^{3+}) and the fO_2 dependence of $D_V^{min/melt}$ is similar for each phase (i.e., $D_V^{cpx/melt}$ and $D_V^{grt/melt}$ decrease in a similar fashion as fO_2 increases). This raises the possibility that $D_V^{cpx/grt}$ may not vary much over a wide range of fO_2. In contrast, V is abundant in rt across a spectrum of fO_2s, including under very oxidizing conditions. Regardless of the exact substitution mechanism for V in rt in our experiments, the important conclusion is that rt can accommodate substantial concentrations of V even under high fO_2, while cpx and grt cannot. Consequently, the relative partitioning of V between rt/cpx and rt/grt should be a strong function of fO_2, while $D_V^{cpx/grt}$ may not be.

We began our analysis by comparing the partitioning of V between rt-grt, rt-cpx and cpx-grt pairs in experiments at 1025–1050 °C over an ~ 8 log unit fO_2 range (Fig. 9). $D_V^{rt/grt}$ and $D_V^{rt/cpx}$ increase linearly as fO_2 increases, reflecting the enhanced solubility of V in rt relative to cpx or grt at high fO_2. $D_V^{rt/cpx}$ and $D_V^{rt/grt}$ vary by factors of ~ 3 and ~ 4, respectively, over the fO_2 range of our experiments, indicating that these parameters should be sensitive to changing fO_2 in eclogitic rocks. In contrast, $D_V^{cpx/grt}$ does not vary as a function of fO_2—the slope of the line fit to this data is

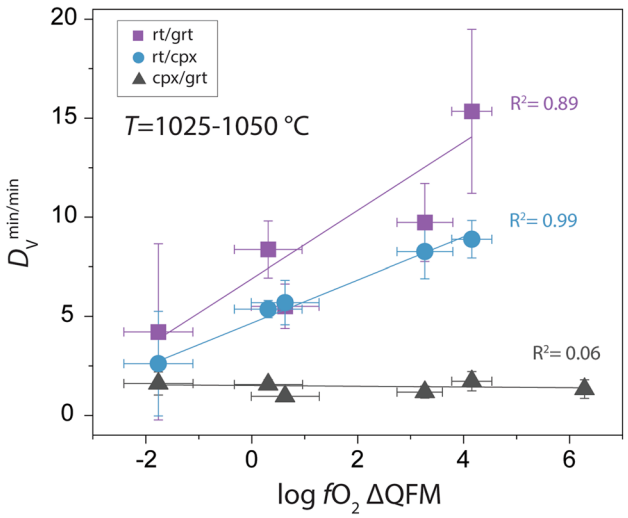

Fig. 9 Partitioning of V between mineral phases at 2 GPa, 1025–1050 °C and varying fO_2. $D_V^{rt/cpx}$ and $D_V^{rt/grt}$ increase linearly with increasing fO_2, reflecting the enhanced solubility of oxidized species of V in rt relative to cpx and grt. $D_V^{cpx/grt}$ changes negligibly as a function of fO_2. Rutile was not found in the experiment at ΔQFM + 6.3

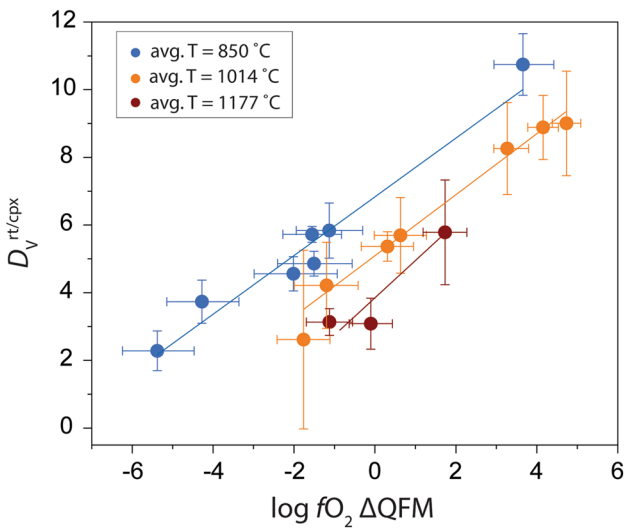

Fig. 10 $D_V^{rt/cpx}$ at varying fO_2. Data are divided into T subgroups for clarity. $D_V^{rt/cpx}$ increases as fO_2 increases and T decreases. At an average constant T, $D_V^{rt/cpx}$ increases 5 × over the ~ 10 log unit fO_2 range of our experiments. Decreasing T by ~ 300 °C drives a ~ 2 × increase in $D_V^{rt/cpx}$ at constant fO_2

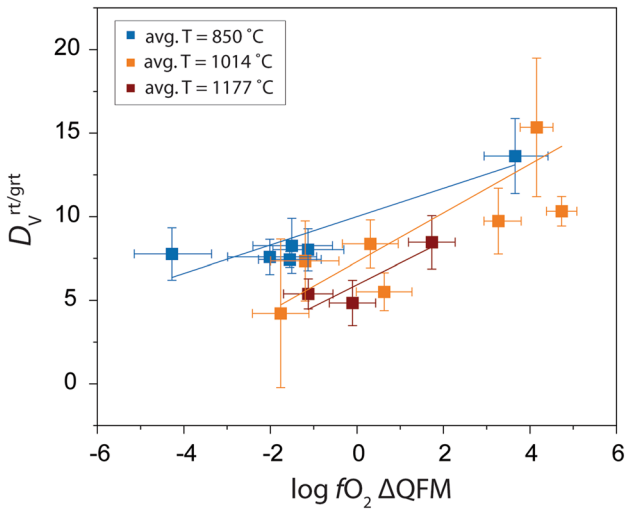

Fig. 11 $D_V^{rt/grt}$ at varying fO_2. Data are divided into T subgroups for clarity. $D_V^{rt/grt}$ generally increases as fO_2 increases and T decreases. Scatter in the plotted data indicates fO_2 and T alone do not fully explain the partitioning of V between rt and grt. See Sect. 5.3 for more details

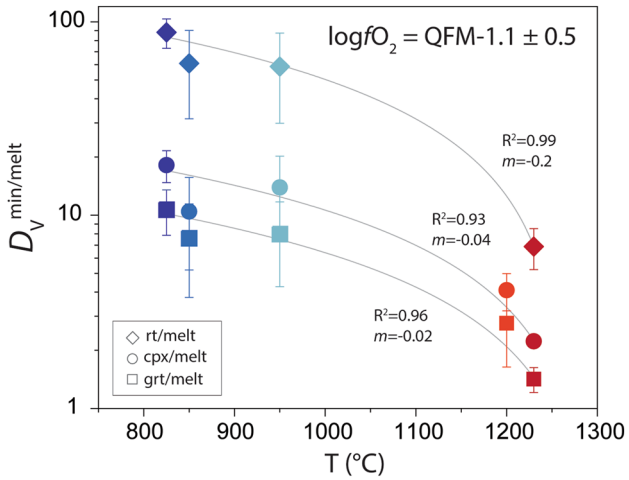

Fig. 12 Temperature dependencies of mineral-melt partition coefficients for V in rt, cpx and grt at a constant average fO_2 of QFM-1.1. Partitioning of V into all phases increases down T, but the slope of the line (m) that describes the temperature dependence of $D_V^{rt/melt}$ is 5 × greater than $D_V^{cpx/melt}$ and 10 × greater than $D_V^{grt/melt}$. The incorporation of V in rt is enhanced at lower T compared to cpx or grt, driving the observed increase of $D_V^{rt/cpx}$ and $D_V^{rt/grt}$. The relationship between T and $D_V^{min/melt}$ at a given fO_2 is linear, but lines are curved on this plot from use of a log scale on the y-axis to improve readability of the data

indistinguishable from zero. Our experiments demonstrate $D_V^{cpx/grt}$ is not suitable for use as an oxybarometer.

After establishing $D_V^{rt/cpx}$ and $D_V^{rt/grt}$ are responsive to changing fO_2 in a subgroup of our experiments, we examined variations in the partitioning of V between rt-cpx and rt-grt pairs in all runs that precipitated rt (800–1230 °C, ΔQFM-5.4 to + 4.7). We divide our experiments into subgroups by T to better illustrate trends in our data set. Figures 10 and 11 show $D_V^{rt/grt}$ and $D_V^{rt/cpx}$ are controlled by both fO_2 and T in our experiments. This indicates V solubility in rt is dependent on T to a greater degree than V solubility in cpx or grt. The T-effect is apparent in a comparison of $D_V^{rt/melt}$, $D_V^{cpx/melt}$ and $D_V^{grt/melt}$ in five experiments run at constant

redox conditions (average fO_2 ΔQFM-1 ± 0.5) and varying T (Fig. 12). The slope of the line that describes the relationship between $D_V^{rt/melt}$ and T is 5 and 10 × greater than the apparent T dependencies of $D_V^{cpx/melt}$ and $D_V^{grt/melt}$, respectively. The net effect is that at constant fO_2, $D_V^{rt/grt}$ and $D_V^{rt/cpx}$ increase with decreasing T. There is also greater scatter present in the $D_V^{rt/grt}$ data, indicating fO_2 and T do not fully explain the partitioning of V between rutile and garnet. All inter-mineral partition coefficients are collated in Table 3.

We parameterized the partitioning of V between rt-cpx and rt-grt pairs at 2 GPa as a function of fO_2, T ± mineral composition:

$$logfO_2 = 0.902\frac{V_{rt}}{V_{cpx}} - \frac{40807}{T} + 17.77 \quad (n = 17, R2 = 0.96, SE = 0.9\text{logunits}) \tag{17}$$

$$logfO_2 = 0.497\frac{V_{rt}}{V_{grt}} - \frac{30463}{T} - 31.90Al + 71.45 \quad (n = 16, R2 = 0.92, SE = 1.1\text{logunits}) \tag{18}$$

where log fO_2 is absolute fO_2 in bars, T is temperature in K, Al is concentration of Al in grt in apfu and V_{rt}, V_{cpx}, and V_{grt} are the measured concentrations of V in each respective phase. All variables in our calibrations are statistically significant at p-values < 0.004. Predicted experiment fO_2s calculated from $D_V^{rt/cpx}$ and $D_V^{rt/grt}$ calibrations are compared to measured experiment fO_2s in Fig. 13. There is excellent agreement between the predicted and measured fO_2s using both calibrations, with small offsets in the most reduced and most oxidized experiments.

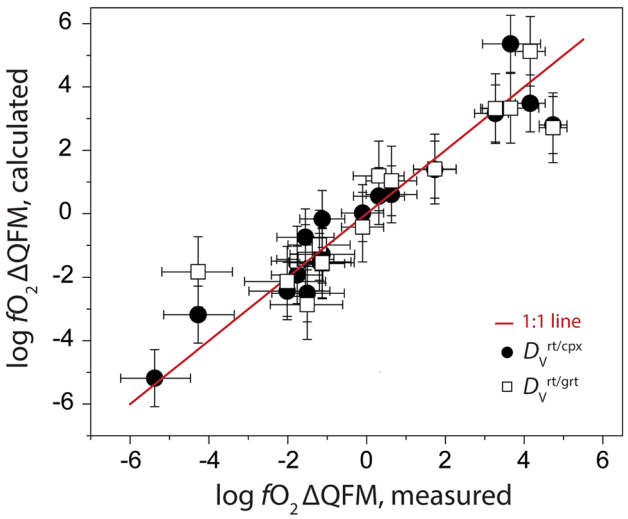

Fig. 13 Measured vs calculated experiment fO_2s determined with $D_V^{rt/cpx}$ and $D_V^{rt/grt}$ calibrations (Eqs. 17 and 18). Agreement between calculated and measured fO_2s using both calibrations is excellent, with small offsets in the most reducing and oxidizing experiments that fall off the 1–1 line

We identify different trends in the inter-mineral partitioning of V that are not apparent in our analysis of $D_V^{min/melt}$

Table 3 V partition coefficients for rt-cpx and rt-grt mineral pairs

Expt#	P	T (°C)	Log f_{O2} ΔQFM[1]	+ log f_{O2} error	− log f_{O2} error	rt/grt	SE	rt/cpx	SE	cpx/grt	SE
1	2	1200	− 1.0	0.50	0.69	No rutile present				1.48	0.68
2	2	1200	− 1.1	0.57	0.57	5.39	0.89	3.13	0.40	1.72	0.31
4	2	1230	− 0.1	0.54	0.54	4.84	1.35	3.09	0.75	1.57	0.24
9	1.8	1150	0.1	0.57	0.58	No rutile present				1.99	0.17
14	2	1025	0.6	0.64	0.65	5.51	1.13	5.70	1.12	0.97	0.15
19	2	1025	4.2	0.38	0.38	15.35	4.15	8.89	0.95	1.73	0.49
20	2	1100	1.7	0.54	0.54	8.47	1.60	5.78	1.55	1.46	0.47
22	2	1050	0.3	0.64	0.65	8.37	1.44	5.37	0.43	1.56	0.25
23	2	1050	− 1.8	0.65	0.65	4.21	4.44	2.61	2.64	1.61	0.58
24	2	1050	3.3	0.53	0.33	9.73	1.97	8.26	1.36	1.18	0.31
27	2	950	4.7	0.35	0.35	10.32	0.88	9.01	1.54	1.15	0.22
31	2	950	− 1.2	0.78	0.80	7.35	2.39	4.22	1.27	1.74	0.45
35	2	850	− 1.1	0.81	0.83	8.02	1.26	5.84	0.81	1.37	0.28
37	2	850	− 4.3	0.87	0.92	7.77	1.57	3.73	0.64	2.08	0.55
38	2	875	3.7	0.71	0.76	13.63	2.24	12.84	3.48	1.06	0.33
39	2	850	− 2.0	0.97	1.08	7.59	1.06	4.56	0.51	1.67	0.28
40	2	825	− 1.5	0.90	0.94	8.25	1.64	4.86	0.37	1.70	0.36
45	2	800	− 5.4	0.86	0.91	53.36	35.40	2.28	0.58	23.38	16.56
46y	2	900	− 1.6	0.72	0.73	7.43	0.47	5.72	0.23	1.30	0.10
47	2	1050	6.3			No rutile present				1.33	0.47

(which included only a subset of our 19 total experiments). We established Al is an important factor in controlling $D_V^{cpx/melt}$ in 12 experiments, but do not find it to be statistically significant in our $D_V^{rt/cpx}$ calibration—fO_2 and T account for 96% of the variance in $D_V^{rt/cpx}$. Similarly, we did not find any impact of grt composition on $D_V^{grt/melt}$ in 12 experiments but found Al in garnet is negatively correlated with $D_V^{rt/grt}$ across all experiments.

Expected effect of pressure

We measured the partitioning of V between cpx, grt, rt and silicate melt over a 10.1 log unit range of fO_2 at 1.8–2 GPa and 825–1230 °C. The one experiment executed at 1.8 GPa yielded only cpx, grt and melt. We do not note any systematic offset in mineral/melt partitioning data from runs at 2 GPa and the one run at 1.8 GPa, perhaps because the difference in P is relatively small. Large deviations in P should impact the relative compatibility of V in rt, cpx and grt as the compressibility of each phase is distinct. The effect of pressure on V compatibility will also be a function of V speciation (and thus the ionic radius) and the size mismatch of the substitution mechanism in each phase. Garnet is generally less compressible than cpx, and rt is much stiffer compared to both phases (Takahashi and Liu 1970; Hazen and Finger 1981; Zhang et al. 1997; Nestola et al. 2006). Our experiments indicate V will swap for Fe^{3+} or Al on the M1 site in cpx and will substitute in grt on the octahedral site in exchange for Al. All species of octahedrally coordinated V are larger than equivalent Al atoms, and the size mismatch increases from 0.9% for V^{5+} to 19.6% for V^{3+}. The opposite is true for V and Fe^{3+}–all species of V are smaller than Fe^{3+}. From the relative sizes of V, Al, Fe coupled with the observation that aegirine is substantially more compressible than jadeite (Nestola et al. 2006), we predict that increasing P will increase the compatibility of all species of V in aegirine and decrease their compatibility in jadeite. If V incorporation in grt occurs primarily via substitution for Al, increasing P should decrease V solubility in garnet. Tetra- and pentavalent V are smaller than Ti^{4+} while V^{3+} is larger than Ti^{4+} but smaller than Ti^{3+}, suggesting increasing P should enhance the incorporation of V in rt under relatively oxidizing conditions.

Notes on relevance of calibrations and application to Koidu eclogite xenolith suite

Although our experiment fO_2s bracket the entire plausible range of subduction zone environments, fO_2 explains only part of the observed variation in our partition coefficients. Much of the variance in our $D_V^{rt/grt}$ and $D_V^{rt/cpx}$ calibrations can be attributed to changing T (and/or the shifts in mineral solid solutions that accompany T changes). To grow crystalline phases large enough to measure with microbeam analytical techniques, and to promote fast kinetic equilibration of V in our in viscous rhyolitic melts (see diffusivities in Holycross and Watson 2018), we had to run our experiments hundreds of degrees hotter than the temperatures encountered on a slab geotherm. Consequently, the major element composition of cpx and grt in our experiments is significantly offset from the compositions of these phases in exhumed metamorphic terranes.

We applied Eqs. 17 and 18 to calculate the fO_2 of eclogitic xenoliths in the ~ 2.7–3.0 Ga Koidu kimberlite complex (Hills and Haggerty 1989; Fung and Haggerty 1995). Koidu xenoliths have previously been interpreted as remnants of early subducted slabs with primary rutile identified in most samples (Barth et al. 2001). While these terranes extend to much higher P than our calibration suite (~ 2.5–7 GPa; Fung and Haggerty 1995; Aulbach et al. 2019b), T estimates for the Koidu xenoliths bracket our experiments (~ 800-1350 °C; Fung and Haggerty 1995; Aulbach et al. 2019b). Previous fO_2 estimates for Koidu xenoliths are published in Aulbach et al. 2019a.

We used LA-ICP-MS data reported in Barth et al. 2001 and Aulbach et al. 2019b to calculate the predicted fO_2s of four Koidu eclogites with our new regressions. Samples K91-4 and K91-11 are low-MgO eclogite xenoliths interpreted by Barth et al. 2001 as metabasalts. Samples K1-16 and K1-18 are hi-Mg and gabbroic eclogite xenoliths, respectively (Aulbach et al. 2019b). Koidu cpx are 64–75 mol% diopside and 18–33 mol% jadeite (Table S19). Koidu garnets are subequal proportions of almandine, grossular and pyrope, with the exception of K1-16 (77 mol% pyrope). Pressure–temperature estimates for K1-16 and K1-18 were calculated iteratively by Aulbach et al. 2019b using the Krogh Ravna 2000 thermometer and the geotherm of Smit et al. 2016. Fung and Haggerty (1995) calculated P–T for K91-4 and K91-11 using the Ellis and Green thermometer (1979) and estimated corresponding P using the Precambrian geotherm of Pollack and Chapman 1977.

Our calculated fO_2s for Koidu are highly variable within the suite and unlikely to be meaningful (Table 4). Oxygen fugacities determined with the $D_V^{rt/grt}$ calibration (Eq. 18) are generally significantly more oxidized than estimates from the $D_V^{rt/cpx}$ calibration (Eq. 17). The fO_2s of K1-16 and K1-18 determined with Eqs. 17 and 18 are three to eight orders of magnitude more oxidized than fO_2s determined by Aulbach et al. 2019a using the unpublished oxybarometer of Vasilyev 2016 (Table 4). The incongruent fO_2s produced with our regressions may be due to application to samples equilibrated outside of our calibrated P–T range; reflect the complex behavior of V in partially metasomatized systems (Fung and Haggerty 1995; Aulbach et al. 2019b); represent disequilibrium among rt, cpx and grt pairs; or may be due to other factors, such as the quality of the published analytical

Table 4 Parameters used in application of Eqs. 17 and 18 to Koidu eclogite xenoliths and calculated fO_2s

Sample	Reference	Eclogite type	T (°C)	P (GPa)	grt X_{Al}	$D_V^{rt/cpx}$	$D_V^{rt/grt}$	ΔQFM (Eq. 17)	ΔQFM (Eq. 18)	ΔQFM* (V16)
K1-16	Aulbach et al. 2019b	hi-Mg	1322	6.6	1.94	8.42	24.73	2.2	5.2	− 3.19
K1-18	Aulbach et al. 2019b	gabbroic	1038	4.8	1.98	8.18	21.31	0.4	1.9	− 2.9
K91-4	Barth et al. 2001	low Mg	908	4.5	1.97	5.04	14.78	− 3.9	− 1.5	–
K91-11	Barth et al. 2001	low Mg	885	3.6	2.00	3.23	7.78	− 5.0	− 5.2	–

*fO_2 estimate using Vasilyev 2016 oxybarometer reported inAulbach et al. 2019a

data and T estimates. In sum, we consider our regressions to show the potential promise of a V-oxybarometer for eclogites, but substantial additional work will be needed before we can assign meaning to the V contents of high-P mineral systems with confidence.

Conclusions

Our new partition coefficients and a critical analysis of the literature data show fO_2 accounts for 50% or less of the observed variance in $D_V^{cpx/melt}$, $D_V^{grt/melt}$ and $D_V^{rt/melt}$. Temperature (and/or compositional effects that are directly related to T) exerts strong control on the partitioning of V between cpx, grt, rt and silicate melt. At constant fO_2 and pressure, decreasing temperature increases the solubility of V in all eclogitic minerals investigated here. V partitioning into cpx, grt and rt is greatest under cold, reducing conditions, but V remains compatible in these phases even under oxidized conditions. We find $D_V^{rt/melt} > D_V^{cpx/melt} > D_V^{grt/melt}$ in all experiments. The high compatibility of V in crystalline phases results in negligible mass transfer of V during eclogite melting or arc cumulate fractionation in subduction zones—melts in equilibrium with these assemblages will be depleted in V compared to melts of the surrounding arc mantle.

Under isothermal and isobaric conditions, the partitioning of V between rt-cpx and rt-grt pairs is positively correlated with fO_2, reflecting the enhanced compatibility of oxidized species of V in rt relative to cpx or grt. Vanadium partitioning in rt is dependent on temperature to a greater degree than partitioning in cpx and grt. This results in an increase in $D_V^{rt/cpx}$ and $D_V^{rt/grt}$ as T decreases at constant fO_2. At constant average T, $D_V^{rt/grt}$ and $D_V^{rt/cpx}$ increase by 4 × and 5 ×, respectively, over a ~ 10 log unit increase in experiment fO_2. At constant average fO_2, $D_V^{rt/cpx}$ and $D_V^{rt/grt}$ increase roughly double as T decreases by ~ 300 °C (Figs. 10 and 11). Redox state will be the dominant influence on $D_V^{min/min}$ over a very large range of fO_2, but over more limited fO_2 shifts, thermal effects become equally as important. Our experiments show the partitioning of V among rt-cpx and rt-grt pairs may theoretically record the redox state of eclogites, but we caution against the application of our calibrations to natural systems without further investigation of V solubility in rt, cpx and grt over a wider range of pressures, temperatures and mineral solid solutions.

Supplementary Information The online version contains supplementary material available at https://doi.org/10.1007/s00410-022-01888-8.

Acknowledgements This study was funded by NSF EAR 1855208 awarded to MH. EC acknowledges funding from the Smithsonian Institution. We thank Tim Gooding and Tim Rose at the Smithsonian and Lyndsey Fisher at Cornell for lab support. We acknowledge the support of GeoSoilEnviroCARS (The University of Chicago, Sector 13), which is supported by the National Science Foundation—Earth Sciences (EAR—1634415) and Department of Energy- GeoSciences (DE-FG02-94ER14466). This research used resources of the Advanced Photon Source, a U.S. Department of Energy (DOE) Office of Science User Facility operated for the DOE Office of Science by Argonne National Laboratory under Contract No. DE-AC02-06CH11357.

References

Adam J, Green TH (1994) The effects of pressure and temperature on the partitioning of Ti, Sr and REE between amphibole, clinopyroxene and basanitic melts. Chem Geol 117:219–233

Adam J, Green T (2006) Trace element partitioning between mica-and amphibole-bearing garnet lherzolite and hydrous basanitic melt: 1. Experimental results and the investigation of controls on partitioning behaviour. Contrib Mineral Petrol 152:1–7

Akella J, Vaidya SN, Kennedy GC (1969) Melting of sodium chloride at pressures to 65 kbar. Phys Rev 185:1135

Arató R, Audétat A (2017) Experimental calibration of a new oxybarometer for silicic magmas based on vanadium partitioning between magnetite and melt. Geochim Cosmochim Acta 209:284–295

Armbruster T, Geiger CA (1993) Andradite crystal chemistry, dynamic X-site disorder and structural strain in silicate garnets. Eur J Mineral 5:59–71

Aulbach S (2020) Temperature-dependent rutile solubility in garnet and clinopyroxene from mantle eclogite: implications for continental crust formation and V-based oxybarometry. J Pet 61:1–26

Aulbach S, Stagno V (2016) Evidence for a reducing Archean ambient mantle and its effects on the carbon cycle. Geology 44:751–754

Aulbach S, Woodland AB, Stern RA, Vasilyev P, Heaman LM, Viljoen KS (2019a) Evidence for a dominantly reducing Archean ambient mantle from two redox proxies, and low oxygen fugacity of deeply subducted oceanic crust. Sci Adv 9:1–11

Aulbach S, Hofer HE, Gerdes A (2019b) High-Mg and low-Mg mantle ecologites from Koidu (West African Craton) linked by Neoproterozoic ultramafic melt metasomatism of subducted Archeaan plateau-like oceanic crust. J Pet 60:723–754

Bai TB, Koster van Groos AF (1999) The distribution of Na, K, Rb, Sr, AL, Ge, Cu, W, Mo, La and Ce between granitic melts and coexisting aqueous fluids. Geochim Cosmochim Acta 63:1117–1131

Bak T, Bogdanoff P, Fiechter S, Nowotny J (2012) Defect engineering of titanium dioxide: full defect disorder. Adv Appl Ceram 111:62–71

Ballaran TB, Carpenter MA, Geiger CA, Koziol AM (1999) Local and structural heterogeneity in garnet solid solutions. Phys Chem Miner 26:554–569

Barr JA, Grove TL (2010) AuPdFe ternary solution model and applications to understanding the fO_2 of hydrous, high-pressure experiments. Contrib Mineral Petrol 160:631–643

Barth MG, Rudnick RL, Horn I, McDonough WF, Spicuzza MJ, Valley JW, Haggerty SE (2001) Geochemistry of xenolithic eclogites from West Africa, Part I: a link between low MgO eclogites and Archean crust formation. Geochim Cosmochim Acta 65:1499–1527

Beard CD, van Hinsburg VJ, Stix J, Wilke M (2019) Clinopyroxene/melt trace element partitioning in sodic alkaline magmas. J Pet 60:1797–1823

Bedard JH (2014) Parameterizations of calcic clinopyroxene-melt trace element partition coefficients. Geochem Geophys Geosys 15:303–336

Blundy JD, Wood BJ (1997) A predictive model for rare earth element partitioning between clinopyroxene and anhydrous silicate melt. Contrib Mineral Petrol 129:166–181

Bromiley G, Hilaret N, McCammon C (2004) Solubility of hydrogen and ferric iron in rutile and TiO_2 (II): implications for phase assemblages during ultrahigh-pressure metamorphism and for the stability of silica polymorphs in the lower mantle. Geophys Res Lett 31:L04610

Burnham CW (1975) Water and magmas: a mixing model. Geochim Cosmochim Acta 39:1077–1084

Cameron M, Papike JJ (1981) Structural and chemical variations in pyroxenes. Am Min 66:1–50

Canil D (1997) Vanadium partitioning and the oxidation state of Archean komatiite magmas. Nature 389:842–845

Canil D (1999) Vanadium partitioning between orthopyroxene, spinel and silicate melt and the redox states of mantle source regions for primary magmas. Geochim Cosmochim Acta 63:557–572

Canil D (2002) Vanadium in peridotites, mantle redox and tectonic environments: Archean to present. Earth Planet Sci Lett 195:75–90

Canil D, Fedortchouk Y (2000) Clinopyroxene-liquid partitioning for vanadium and the oxygen fugacity during formation of cratonic and oceanic mantle lithosphere. J Geophys Res 105:26003–26016

Canil D, Fedortchouk Y (2001) Olivine-liquid partitioning of vanadium and other trace elements, with applications to modern and ancient picrites. Canad Mineral 39:319–330

Carmichael ISE (1991) The redox states of basic and silicic magmas: a reflection of their source regions? Contrib Mineral Petrol 106:169–141

Colasanti CV, Johnson EA, Manning CE (2011) An experimental study of OH solubility in rutile at 500–900 C, 0.5-2 GPa and a range of oxygen fugacities. Am Min 96:1291–1299

Cottrell E, Kelley KA, Lanzirotti A, Fischer RA (2009) High-precision determination of iron oxidation state in silicate glasses using XANES. Chem Geol 268:167–179

Cottrell E, Lanzirotti A, Mysen B, Birner S, Kelley KA, Botcharnikov R, Davis FA, Newville M (2018) A Mössbauer-based XANES calibration for hydrous basaltic glasses reveals radiation-induced oxidation of Fe. Am Min 103:489–501

Cottrell E, Birner S, Brounce M, Davis FA, Waters LE, Kelley KA (2021) Oxygen fugacity across tectonic settings. In: Neuville DR, Moretti R (eds) AGU geophysical monograph Redox variables and mechanisms in magmatism and volcanis. Wiley, Hoboken

Davis F, Cottrell E (2021) Partitioning of Fe2O3 in peridotite partial melting experiments over a range of oxygen fugacities elucidates ferric iron systematics in mid-ocean ridge basalts and ferric iron content of the upper mantle. Contrib Mineral Petrol. https://doi.org/10.1007/s00410-021-01823-3 (**In press**)

Defant MJ, Drummond MS (1990) Derivation of some modern arc magmas by melting of young subducted lithosphere. Nature 347:662–665

Donohue CL, Essene EJ (2000) An oxygen barometer with the assemblage garnet-epidote. Earth Planet Sci Lett 181:459–472

Ducea MN, Saleeby JB, Bergantz G (2015) The architecture, chemistry and evolution of continental magmatic arcs. Ann Rev Earth Planet Sci 43:299–331

Dygert N, Liang Y, Hess P (2013) The importance of melt TiO2 in affecting major and trace element partitioning between Fe–Ti oxides and lunar picritic glass melts. Geochim Cosmochim Acta 106:134–151

Ellis DJ, Green DH (1979) An experimental study of the effect of Ca upon garnet-clinopyroxene Fe–Mg exchange equilibria. Contrib Mineral Petrol 71:13–22

Eugster HP (1957) Heterogeneous reactions involving oxidation and reduction at high pressures and temperatures. J Chem Phys 26:1760–1761

Foley SF, Barth MG, Jenner GA (2000) Rutile/melt partition coefficients for trace elements and an assessment of the influence of rutile on the trace element characteristics of subduction zone magmas. Geochim Cosmochim Acta 64:933–938

Francis D, Minarik W (2008) Aluminum-dependent trace element partitioning in clinopyroxene. Contrib Mineral Petrol 156:439–451

Frost BR (1991) Introduction to oxygen fugacity and its petrologic importance. Rev Mineral Geochem 25:1–9

Fung AT, Haggerty SE (1995) Petrography and mineral compositions of eclogites from the Koidu kimberlite complex, Sierra Leone. J Geophys Res 100:451–473

Gaetani GA (2004) The influence of melt structure on trace element partitioning near the peridotite solidus. Contrib Mineral Petrol 147:511–527

Gaetani GA, Grove TL (1995) Partitioning of rare earth elements between clinopyroxene and silicate melt Crystal-chemical controls. Geochim Cosmochim Acta 59:1951–1962

Gale A, Dalton CA, Langmuir CH, Su Y, Schilling J (2013) The mean composition of ocean ridge basalts. Geochem Geophys Geosystems 14:489–518

Green TH, Adam J (2003) Experimentally- determined trace element characteristics of aqueous fluid from partially dehydrated mafic oceanic crust at 3.0 GPa, 650–700 C. Eur J Mineral 15:815–830

Green TH, Pearson NJ (1985) Rare earth element partitioning between clinopyroxene and silicate liquid at moderate to high pressure. Contrib Mineral Petrol 91:24–36

Gudmundsson G, Holloway JR (1993) Activity-composition relationships in the system Fe–Pt at 1300 and 1400 C and at 1 atm and 20 kbar. Am Min 78:178–186

Hazen RM, Finger LW (1981) Bulk moduli and high-pressure crystal structures of rutile-type compounds. J Phys Chem Solids 42:143–151

Hermann J (2002) Allanite: thorium and light rare earth element carrier in subducted crust. Chem Geol 192:289–306

Hill E, Wood BJ, Blundy JD (2000) The effect of Ca-Tschermaks component on trace element partitioning between clinopyroxene and silicate melt. Lithos 53:203–215

Hills DV, Haggerty SE (1989) Petrochemistry of eclogites from the Koidu Kimberlite Complex, Sierra Leone. Contrib Mineral Petrol 103:397–422

Hoff C (2019) Defect thermometry using rutile and feldspar. Ph.D. thesis, Rensselaer Polytechnic Institute

Holycross M, Cottrell E (2020) Partitioning of V and 19 other trace elements between rutile and silicate melt as a function of oxygen fugacity and melt composition: Implications for subduction zones. Am Min 105:244–254

Holycross ME, Watson EB (2018) Trace element diffusion and kinetic fractionation in wet rhyolitic melt. Geochim Cosmochim Acta 232:14–29

Hughes EC, Buse B, Kearns SL, Blundy JD, Kilgour G, Mader HM (2019) Low analytical totals in EPMA of hydrous silicate glass due to sub-surface charging: obtaining accurate volatiles by difference. Chem Geol 505:48–56

Jochum KP, Willbold M, Raczek I, Stoll B, Herwig K (2005) Chemical characterization of the USGS reference glasses GSA-1G, GSC-1G, GSD-1G, GSE-1G, BCR-2G, BHVO-2G and BIR-1G Using EPMA, ID-TIMS, ID-ICP-MS and LA-ICP-MS. Geostand Geoanal Res 29:285–302

Jochum KP, Weis U, Stoll B, Kuzmin D, Yang Q, Raczek I, Jacob DE, Stracke A, Birbaum K, Frick DA, Gunther D (2011) Determination of reference values of NIST SRM 610–617 glasses following ISO guidelines. Geostand Geoanal Res 35:397–429

Karner JM, Papike JJ, Sutton SR, Shearer CK, Burger P, McKay G, Le L (2008) Valence state partitioning of V between pyroxene-melt: Effects of pyroxene and melt composition, and direct determination of V valence states by XANES. Application to Martian basalt QUE 94201 composition. Meteorit Planet Sci 8:1275–1285

Kessel R, Beckett JR, Stolper EM (2001) Thermodynamic properties of the Fe–Pt system. Am Min 86:1003–1014

Klemme S, Prowatke S, Hametner K, Günther D (2005) Partitioning of trace elements between rutile and silicate melts: implications for subduction zones. Geochim Cosmochim Acta 69:2361–2371

Kress VC, Carmichael IS (1991) The compressibility of silicate liquids containing Fe2O3 and the effect of composition, temperature, oxygen fugacity and pressure on their redox states. Contrib Mineral Petrol 108:82–92

Krogh Ravna E (2000) The garnet-clinopyroxene Fe^{2+}-Mg geothermometer: an updated calibration. J Metamorph Geol 18:211–219

Kushiro I (1960) Si-Al relation in clinopyroxenes from igneous rocks. Am J Sci 258:548–554

Lanzirotti A, Dyar MD, Sutton S, Newville M, Head E, Carey CJ, McCanta M, Lee L, King PL, Jones J (2018) Accurate predictions of microscale oxygen barometry in basaltic glasses using V K-edge X-ray absorption spectroscopy: a multivariate approach. Am Min 103:1282–1297

Laubier M, Grove TL, Langmuir CH (2014) Trace element mineral/melt partitioning for basaltic and basaltic andesitic melts: an experimental and laser ICP-MS study with application to the oxidation state of mantle source regions. Earth Planet Sci Lett 392:265–278

Lee CTA, Leeman WP, Canil D, Li ZXA (2005) Similar V/Sc systematics in MORB and arc basalts: implications for the oxygen fugacities of their mantle source regions. J Pet 46:2313–2336

Leitzke FP, Fonesca ROC, Michely LT, Sprung P, Munker C, Heuser A, Blanchard H (2016) The effect of titanium on the partitioning behavior of high-field strength elements between silicates, oxides and lunar basaltic melts with applications to the origin of mare basalts. Chem Geol 440:219–238

Liu L, Xioa Y, Aulbach S, Li D, Hou Z (2014) Vanadium and niobium behavior in rutile as a function of oxygen fugacity: evidence from natural samples. Contrib Mineral Petrol 167:1026

Lundstrom CC, Shaw HF, Ryerson FJ, Phinney DL, Gill JB, Williams Q (1994) Compositional controls on the partitioning of U, Th, Ba, Pb, Sr and Zr between clinopyroxene and haplobasaltic melts: implications for uranium series disequlibria in basalts. Earth Planet Sci Lett 128:407–423

Mallmann G, O'Neill HSC (2007) The effect of oxygen fugacity on the partitioning of Re between crystals and silicate melt during mantle melting. Geochim Cosmochim Acta 71:2837–2857

Mallmann G, O'Neill HSC (2009) The crystal/melt partitioning of V during mantle melting as a function of oxygen fugacity compared with some other elements (Al, P, Ca, Sc, Ti, Cr, Fe, Ga, Y, Zr and Nb). J Pet 50:1765–1794

Mallmann G, O'Neill HSC (2013) Calibration of an empirical thermometer and oxybarometer based on the partitioning of Sc, Y and V between olivine and silicate melt. J Pet 54:933–949

Mallmann G, Fonesca ROC, Silva AB (2014) An experimental study of the partitioning of rutile and silicate melt as a function of oxygen fugacity. An Acad Bras Cienc 86:1609–1629

Martin H (1986) Effect of steeper Archean geothermal gradient on geochemistry of subduction-zone magmas. Geology 14:753–756

Matjuschkin V, Brooker RA, Tattitch B, Blundy JD, Stamper CC (2015) Control and monitoring of oxygen fugacity in piston cylinder experiments. Contrib Mineral Petrol 169:9

Mollo S, Vona A (2014) The geochemical evolution of clinopyroxene in the Roman Province: a window on decarbonation from wall-rocks to magma. Lithos 192:1–7

Mollo S, Blundy J, Scarlato P, Vetere F, Holtz F, Bachmann O, Gaeta M (2020) A review of the lattice strain and electrostatic effects on trace element partitioning between clinopyroxene and melt: applications to magmatic systems saturated with Tschermak-rich clinopyroxenes. Earth Sci Rev 210:103351

Nestola F, Tribaudino M, Boffa Ballaran T, Liebske C, Bruno M (2006) The crystal structure of pyroxenes along the jadeite-hedenbergite and jadeite-aegerine joins. Am Min 92:1492–1501

Nicklas RW, Puchtel IS, Ash RD (2016) High-precision determination of the oxidation state of komatiite lavas using vanadium liquid-mineral partitioning. Chem Geol 433:36–45

Nicklas RW, Puchtel IS, Ash RD, Piccoli PM, Hanski E, Nisbet EG, Waterton P, Pearson DG, Anbar AD (2019) Secular mantle oxidation across the Archean-Proterozoic boundary: evidence from V partitioning in komatiites and picrites. Geochim Cosmochim Acta 25:49–75

Nicklas RW, Day JMD, Vaci Z, Udry A, Liu Y, Tait KT (2021) Uniform oxygen fugacity of shergottite mantle sources and an oxidized martian lithosphere. Earth Planet Sci Lett 564:116876

Novella D, Maclennan J, Shorttle O, Prytulak J (2020) A multi-proxy investigation of mantle oygen fugacity along the Reykjanes Ridge. Earth Planet Sci Lett 531:115973

O'Neill HSC, Eggins SM (2002) The effect of melt composition on trace element partitioning: an experimental investigation of the activity coefficients of FeO, NiO, CoO, MoO2 and MoO3 in silicate melts. Chem Geol 186:151–181

O'Neill HSC, Berry AJ, McCammon CC, Jayasuriya KD, Campbell SJ, Foran G (2006) An experimental determination of the effect of pressure on the $Fe^{3+}/\sum Fe$ ratio of an anhydrous silicate melt to 3.0 GPa. Am Min 91:404–412

Ohtani E, Kawabe I, Moriyama J, Nagata Y (1989) Partitioning of elements between majorite garnet and melt and implications for petrogenesis of komatiite. Contrib Mineral Petrol 103:263–269

Papike JJ, Burger PV, Bell AS, Shearer CK, Le L, Jones J, Provencio P (2014) Valence state partitioning of V between pyroxene and melt for Martian melt compositions Y 980459 and QUE 94201: the effect of pyroxene composition and crystal structure. Am Min 99:175–1178

Pertermann M, Hirschmann MM (2002) Trace-element partitioning between vacancy-rich eclogitic clinopyroxene and silicate melt. Am Min 87:1365–1376

Poli S, Schmidt MW (2002) Petrology of subducted slabs. Ann Rev Earth Planet Sci 30:207–235

Pollack HN, Chapman DS (1977) On the regional variation of heat flow, geotherms, and lithospheric thickness. Tectonophys 38:279–296

Rapp RP, Watson EB (1995) Dehydration melting of metabasalt at 8–32 kbar: implications for continental growth and crust-mantle recycling. J Pet 36:891–931

Redhammer GJ, Amthauer G, Roth G, Tippelt G, Lottermoser W (2006) Single-crystal X-ray diffraction and temperature dependent ^{57}Fe Mossbauer spectroscopy on the hedenbergite-aegerine (Ca, Na) (Fe^{2+}, Fe^{3+})Si_2O_6 solid solution. Am Min 91:1271–1292

Righter K, Sutton SR, Newville M, Le L, Schwandt CS, Uchida H, Lavina B, Downs RT (2006) An experimental study of the oxidation state of vanadium in spinel and basaltic melt with implications for the origin of planetary basalt. Am Min 91:1643–1656

Righter K, Sutton S, Danielson L, Pando K, Schmidt G, Yang H, Berthet S, Newville M, Choi Y, Downs RT, Malavergne V (2011) The effect of fO2 on the partitioning and valence of V and Cr in garnet/melt pairs and the relation to terrestrial mantle V and Cr content. Am Min 96:1278–1290

Ryerson FJ, Watson EB (1987) Rutile saturation in magmas: implications forTi-Nb-Ta depletion in island-arc basalts. Earth Planet Sci Lett 86:225–239

Schmidt MW, Dardon A, Chazot G, Vannucci R (2004) The dependence of Nb and Ta rutile-melt partitioning on melt composition and Nb/Ta fractionation during subduction processes. Earth Planet Sci Lett 226:415–432

Schreiber HD (1986) An electrochemical series of redox couples in silicate melts: a review and applications to geochemistry. J Geophys Res 92:9225–9232

Shannon RD (1976) Revised effective ionic radii and systematic studies of interatomic distances of halides and chalcogenides. Act Cryst A 32:751–767

Shervais JW (1982) Ti-V plots and the petrogenesis of modern and ophiolitic lavas. Earth Planet Sci Lett 59:101–118

Shishkina TA, Portnyagin MV, Botcharnikov RE, Almeev RR, Simonyan AV, Garbe-Shönberg D, Schuth S, Oeser M, Holtz F (2018) Experimenal calibration and implications of olivine-melt vanadium oxybarometry for hydrous basaltic arc magmas. Am Min 103:369–383

Sisson TW, Kelemen PB (2018) Near solidus melts of MORB + 4 wt% H2O at 0.8-2.8 GPa applied to issues of subduction magmatism and continent formation. Contrib Mineral Petrol 9:1–23

Smit KV, Shirey SB, Wang WY (2016) Type Ib diamond formation and preservation in the West African lithospheric mantle: Re-Os age constraints from sulphide inclusions in Zimmi diamonds. Precambrian Res 286:152–166

Snetsinger KG, Bunch TE, Keil K (1968) Electron microprobe analysis of vanadium in the presence of titanium. Am Min 53:1770–1773

Sossi PA, Prytulak J, O'Neill HSC (2018) Experimental calibration of vanadium partitioning and stable isotope fractionation between hydrous granitic melt and magnetite and 800 C and 0.5 GPa. Contrib Mineral Petrol 173:1–18

Spandler C, Mavrogenes J, Hermann J (2007) Experimental constraints on element mobility from subducted sediments using high-P synthetic fluid/melt inclusions. Chem Geol 239:228–249

Stagno V, Frost DJ, McCammon CA, Mohseni H, Fei Y (2015) The oxygen fugacity at which graphite or diamond forms from carbonate-bearing melts in eclogitic rocks. Contrib Mineral Petrol 169:16

Stolper DA, Bucholz CE (2019) Neoproterozoic to early Phanerozoic rise in island arc redox state due to deep ocean oxygenation and increased marine sulfate levels. Proc Natl Acad Sci USA 116:8746–8755

Sutton SR, Karner J, Papike J, Delaney JS, Shearer C, Newville M, Eng P, Rivers M, Dyar MD (2005) Vanadium K edge XANES of synthetic and natural basaltic glasses and application to microscale oxygen barometry. Geochim Cosmochim Acta 69:2333–2348

Syracuse EM, van Keken PE, Abers GA (2010) The global range of subduction zone thermal models. Phys Earth Planet Inter 183:73–90

Takahashi T, Liu LG (1970) Compression of ferromagnesian garnets and the effect of solid solutions on the bulk modulus. J Geophys Res 75:5757–5766

Toplis MJ, Corgne A (2002) An experimental study of element partitioning between magnetite, clinopyroxene and iron-bearing silicate liquids with particular emphasis on vanadium. Contrib Mineral Petrol 144:22–37

Vasilyev P (2016) The oxidation state of deeply subducted, altered oceanic crust: an experimental study and the evidence from natural samples. PhD thesis, Australian National University

Wang J, Xiong X, Takahashi E, Zhang L, Li L, Liu X (2019) Oxidation state of arc mantle revealed by partitioning of V, Sc, and Ti between mantle minerals and basaltic melts. J Geophys Res Solid Earth 124:4617–4638

Whitney DL, Evans BW (2010) Abbreviations for names of rock-forming minerals. Am Min 95:185–187

Wood BJ, Blundy JD (2001) The effect of cation charge on crystal-melt partitioning of trace elements. Earth Planet Sci Lett 188:59–71

Xiong XL, Adam J, Green TH (2005) Rutile stability and rutile/melt HFSE partitioning during partial melting of hydrous basalt: implications for TTG genesis. Chem Geol 218:339–359

Xirouchakis D, Hirschmann MM, Simpson JA (2001) The effect of titanium on the silica content and on mineral-liquid partitioning of mantle-equilibrated melts. Geochim Cosmochim Acta 65:2201–2217

Zhang L, Ahsbahs H, Hafner SS, Kutoglu A (1997) Single-crystal compression and crystal structure of clinopyroxene up to 10 GPa. Am Min 82:245–258

Zhang HL, Hirschmann MM, Cottrell E, Newville M, Lanzirotti A (2016) Structural environment of iron and accurate determination of Fe3+/ΣFe ratios in andesitic glasses by XANES and Mossbauer spectroscopy. Chem Geol 428:48–58

Zhang HL, Cottrell E, Solheid PA, Kelley KA, Hirschmann MM (2018) Determination of the Fe3+/ΣFe of XANES basaltic glass standard by Mössbauer spectroscopy and its application to the oxidation state of iron in MORB. Chem Geol 479:166–175

Zhao D, Essene EJ, Zhang Y (1999) An oxygen barometer for rutile-ilmenite assemblages: oxidation state of metasomatic agents in the mantle. Earth Planet Sci Lett 166:127–137